

# Distinct features of calcium handling and $\beta$ -adrenergic sensitivity in heart failure with preserved versus reduced ejection fraction

Peter J. Kilfoil<sup>1</sup>, Sabine Lotteau<sup>1</sup>, Rui Zhang<sup>1</sup>, Xin Yue<sup>2</sup>, Stephan Aynaszyan<sup>1</sup>, Ryan E. Solymani<sup>1</sup>, Eugenio Cingolani<sup>1</sup>, Eduardo Marbán<sup>1</sup> and Joshua I. Goldhaber<sup>1</sup> 

<sup>1</sup>Cedars-Sinai Medical Center, Smidt Heart Institute, Los Angeles, CA, USA

<sup>2</sup>Department of Cardiovascular Medicine, First Affiliated Hospital of Xi'an Jiaotong University, Xi'an, Shaanxi, China

Edited by: Don Bers & Robert Harvey

Linked articles: This article is highlighted in a Perspectives article by Louch and a Journal Club article by Durland. To read these articles, visit <https://doi.org/10.1113/JP280691> and <https://doi.org/10.1113/JP280739>.

## Key points

- Heart failure (HF), the leading cause of death in developed countries, occurs in the setting of reduced (HFrEF) or preserved (HFpEF) ejection fraction. Unlike HFrEF, there are no effective treatments for HFpEF, which accounts for ~50% of heart failure.
- Abnormal intracellular calcium dynamics in cardiomyocytes have major implications for contractility and rhythm, but compared to HFrEF, very little is known about calcium cycling in HFpEF.
- We used rat models of HFpEF and HFrEF to reveal distinct differences in intracellular calcium regulation and excitation-contraction (EC) coupling.
- While HFrEF is characterized by defective EC coupling at baseline, HFpEF exhibits enhanced coupling fidelity, further aggravated by a reduction in  $\beta$ -adrenergic sensitivity.
- These differences in EC coupling and  $\beta$ -adrenergic sensitivity may help explain why therapies that work in HFrEF are ineffective in HFpEF.

**Abstract** Heart failure with reduced or preserved ejection fraction (respectively, HFrEF and HFpEF) is the leading cause of death in developed countries. Although numerous therapies improve outcomes in HFrEF, there are no effective treatments for HFpEF. We studied phenotypically verified rat models of HFrEF and HFpEF to compare excitation-contraction (EC) coupling and protein expression in these two forms of heart failure. Dahl salt-sensitive rats were fed a high-salt diet (8% NaCl) from 7 weeks of age to induce HFpEF. Impaired diastolic relaxation and preserved ejection fraction were confirmed in each animal echocardiographically, and clinical signs of heart failure were documented. To generate HFrEF, Sprague-Dawley (SD) rats underwent permanent left anterior descending coronary artery ligation which, 8–10 weeks later, led to

**Peter Kilfoil** undertook predoctoral training in ion channel physiology at the University of Louisville, following which he came to the Smidt Heart Institute at Cedars-Sinai Medical Center in Los Angeles to investigate the electrophysiological changes that occur in HFpEF. With an initial hypothesis that he would see predominantly diastolic changes, he soon uncovered unanticipated changes in systolic calcium handling as well, some of which can be explained by altered  $\beta$ -adrenergic responses. Further investigating the signalling changes responsible for this altered systolic function is a future goal and may provide important insights into this disease.



systolic dysfunction (verified echocardiographically) and clinical signs of heart failure. Calcium ( $\text{Ca}^{2+}$ ) transients were measured in isolated cardiomyocytes under field stimulation or patch clamp. Ultra-high-speed laser scanning confocal imaging captured  $\text{Ca}^{2+}$  sparks evoked by voltage steps. Western blotting and PCR were used to assay changes in EC coupling protein and RNA expression. Cardiomyocytes from rats with HFrEF exhibited impaired EC coupling, including decreased  $\text{Ca}^{2+}$  transient (CaT) amplitude and defective couplon recruitment, associated with transverse (t)-tubule disruption. In stark contrast, HFpEF cardiomyocytes showed saturated EC coupling (increased  $I_{\text{Ca}}$ , high probability of couplon recruitment with greater  $\text{Ca}^{2+}$  release synchrony, increased CaT) and preserved t-tubule integrity.  $\beta$ -Adrenergic stimulation of HFpEF myocytes with isoprenaline (isoproterenol) failed to elicit robust increases in  $I_{\text{Ca}}$  or CaT and relaxation kinetics. Fundamental differences in EC coupling distinguish HFrEF from HFpEF.

(Received 7 July 2020; accepted after revision 19 August 2020; first published online 23 August 2020)

**Corresponding author** J. I. Goldhaber, Smidt Heart Institute at Cedars-Sinai Medical Center, 8700 Beverly Blvd, Los Angeles, CA 90048, USA. Email: joshua.goldhaber@cshs.org

## Introduction

Heart failure – a syndrome marked by pulmonary congestion and exercise intolerance – is the leading cause of hospitalization and death in developed countries (Shah *et al.* 2017; Lam *et al.* 2018). Two entirely different pathophysiological entities produce heart failure. The better-understood entity is heart failure with reduced ejection fraction (HFrEF), in which the heart is dilated and contracts poorly; the second, heart failure with preserved ejection fraction (HFpEF), is characterized by impaired relaxation without dilatation. Patients exhibit similar signs and symptoms regardless of the cause (Pieske *et al.* 2019). Although numerous drugs and devices have been proven effective in HFrEF, there are no effective treatments for HFpEF, which accounts for ~50% of heart failure (Dunlay *et al.* 2017). It is well established that abnormal  $\text{Ca}^{2+}$  regulation and defective excitation-contraction (EC) coupling underlie abnormal contractility in HFrEF. Common features in human and animal models of HFrEF include reduction in the  $\text{Ca}^{2+}$  transient (CaT) amplitude, slowing of CaT decay, increased sarcoplasmic reticulum (SR)  $\text{Ca}^{2+}$  leak through phosphorylated RyRs, increased  $\text{Ca}^{2+}$  efflux by  $\text{Na}^+/\text{Ca}^{2+}$  exchange (NCX) and depleted SR  $\text{Ca}^{2+}$  (Zima *et al.* 2014). Much less is known about  $\text{Ca}^{2+}$  regulation in HFpEF, but an unproven assumption is that slowed SR  $\text{Ca}^{2+}$  uptake is the dominant cause of diastolic dysfunction, the signature feature of HFpEF haemodynamics (Cain *et al.* 1998; Ouzounian *et al.* 2008; Zile & Gaasch, 2011). Here we used phenotypically verified rat models of HFpEF and HFrEF to uncover distinct differences in EC coupling and  $\text{Ca}^{2+}$  regulation between these two forms of heart failure. We found that differences in the subcellular mechanism of EC coupling and  $\beta$ -adrenergic sensitivity distinguish systolic abnormalities in HFrEF from those present in HFpEF, and help explain why HFrEF-targeted interventions to improve contractile function have largely failed when applied to HFpEF patients.

## Methods

### Ethical approval

All animal care and experiments conform to the principles and regulations as described in the editorial by Grundy (2015), were in accordance with institutional guidelines and approved by the Cedars-Sinai Institutional Animal Care and Use Committee (IACUC005280), and adhered to the *Guide for the Care and Use of Laboratory Animals* prepared by the Committee for the Update of the Guide for the Care and Use of Laboratory Animals of the Institute of Laboratory Animal Research, National Research Council (US).

### Animal models of HFpEF and HFrEF

Animals were housed by the Cedars-Sinai Department of Comparative Medicine, which is fully accredited by the AAALAC International (Association for the Assessment and Accreditation of Laboratory Animal Care), under a 10 h:14 h dark/light cycle. Lights were switched on at 06.00 h and off at 20.00 h. The ambient room temperature was maintained at 20–25°C. Humidity was not controlled.

We implemented the Dahl salt-sensitive (DS) rat model of HFpEF as described previously (Fig. 1A) (Gallet *et al.* 2016). Briefly, 7-week-old male DS rats (Charles River Laboratories, MA, USA) underwent baseline transthoracic echocardiography under 2.5% isoflurane anaesthesia and were then randomly assigned for 11 weeks to either a high-salt diet (AIN-76A plus 8% NaCl, Research Diets, NJ, USA) to induce hypertension or a normal-salt diet (AIN-76A plus 0.3% NaCl) to serve as controls. Chow and water were available *ad libitum*. At endpoint (after 11 weeks), only high-salt-fed rats with preserved EF (above 65%), diastolic dysfunction confirmed by either elevated  $E/e'$  ratio and/or abnormal  $E/A$  ratio (reduced  $E/A$  or  $E/A$  pseudonormalization) and a clinical heart failure score

>2 (Cho *et al.* 2018b), were selected for experimentation. In our previous studies, we found that mortality of high-salt-fed rats over the high-salt feeding period was ~50% (Gallet *et al.* 2016; Cho *et al.* 2018b). The vast majority (~90%) of surviving rats qualified for use based upon the above criteria. As we reported (Cho *et al.* 2018a), about 17% of mortality is attributable to sudden cardiac death, while the rest is due to non-cardiac causes (seizures, anorexia). There was no evidence of stroke in rats used in our study by gross necropsy.

The rat post-infarct model of HFrEF was generated as described (Pfeffer *et al.* 1979; Terrovitis *et al.* 2009; Wang *et al.* 2016) in animals aged 9–10 weeks. Briefly, male Sprague-Dawley (SD) rats were anaesthetized under 4% isoflurane and the heart was exposed by thoracotomy. The left anterior descending coronary artery was permanently ligated to induce myocardial infarction, the chest was closed and animals were allowed to recover. We administered carprofen (5 mg kg<sup>-1</sup>) subcutaneously after anaesthesia induction to provide post-operative

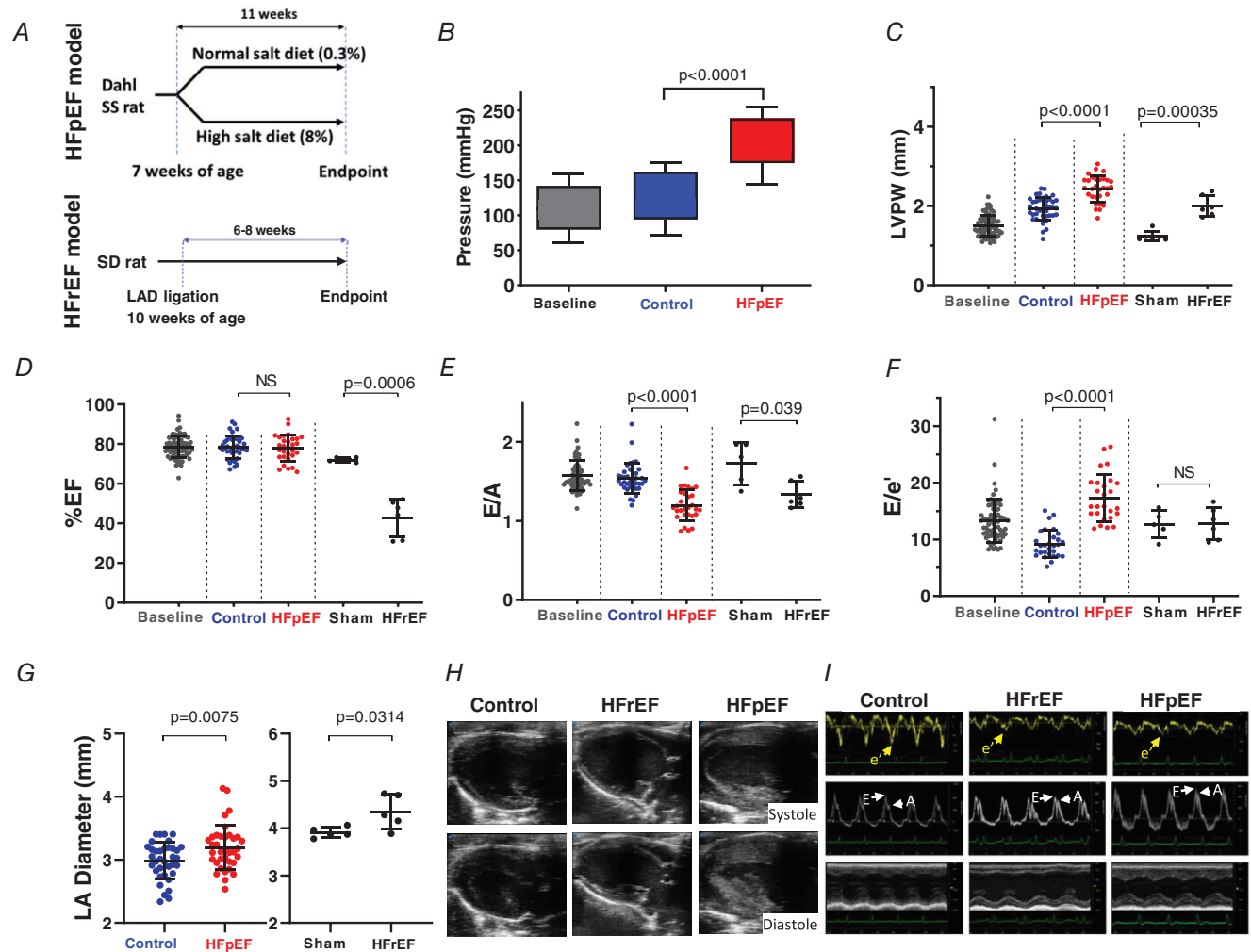


**Figure 1. Generation and characteristics of rat models of HFpEF and HFrEF**  
**A**, HFpEF model: Dahl salt-sensitive (SS) rats were fed a high-salt diet (8% NaCl) or a normal-salt diet (0.3% NaCl) starting at 7 weeks of age. We obtained echocardiograms at baseline and 11 weeks later at endpoint immediately before use in experiments. HFrEF model: Sprague-Dawley (SD) rats underwent permanent ligation of the left anterior descending (LAD) coronary artery or sham procedure. Echocardiograms were performed at baseline and endpoint. **B**, systolic and diastolic blood pressures measured using tail cuff photoplethysmography. Top of filled bar indicates mean systolic pressure (+ SD), bottom of bar indicates mean diastolic pressure (– SD). **C–G**, echo-derived measures including left ventricular (LV) posterior wall thickness at diastole (LVPW), ejection fraction (%EF), E wave to A wave (E/A) ratio, E wave to e' (E/e') ratio, and left atrial (LA) diameter in control, HFrEF and HFpEF. **H**, representative B-mode echo images showing left ventricular end diastole and end systole in control, HFrEF and HFpEF. **I**, representative tissue Doppler, pulse-wave Doppler at mitral annulus and M-mode echo recordings in control, HFrEF and HFpEF. Results are shown as means ± SD. Statistics are calculated by one-way ANOVA (**B–F**) and Student's *t* test (**G**). [Colour figure can be viewed at [wileyonlinelibrary.com](http://wileyonlinelibrary.com)]

analgesia. Chow (PicoLab Rodent Diet 20; LabDiet, St Louis, MO, USA) and water were available *ad libitum*. Following 8–10 weeks of chronic adaptation to the infarct, reduced EF (EF% < 50) was confirmed by echocardiography. Mortality was 14% over 10 weeks. For echocardiographic comparison, a separate group of animals underwent a sham procedure.

### Transthoracic echocardiography

We used Doppler/echocardiography to measure systolic and diastolic function as described (Cho *et al.* 2017). Rats were rapidly anaesthetized under 5% isoflurane and maintained under 2.5% isoflurane for transthoracic echocardiography (Vevo 3100, VisualSonics, Toronto, Canada) on a heated platform with paw electrodes to measure surface ECG (electrocardiogram). Systolic function was assessed by calculating EF from M-mode images obtained in the parasternal short axis view. LA diameter was measured from B-mode images obtained in the parasternal long axis view. Diastolic function was assessed by calculating E/A and E/e' ratios from an apical 4-chamber view. To measure E wave (representing early, passive ventricular filling) and A wave (representing late, atrial-assisted ventricular filling) velocities, we used pulse-wave Doppler mode, placed at the tip of the mitral valve, to record mitral inflow velocity. To assess e' wave velocity, tissue Doppler mode was used at the septal aspect of the mitral annulus. Each measurement was repeated 3 times and analysed offline.

### Cardiomyocyte isolation

We enzymatically isolated adult rat left ventricular cardiomyocytes using a modification of our atrial myocyte isolation protocol (Yue *et al.* 2017). Following intraperitoneal injection with heparin sodium (1000 IU), rats were anaesthetized under 5% isoflurane, the heart was quickly excised by thoracotomy, placed in ice-cold phosphate buffered saline (PBS) and transferred to a Langendorff system. After cannulation, the aorta was retrogradely perfused at a constant flow rate of 9 ml min<sup>-1</sup> with oxygen-bubbled, Ca<sup>2+</sup>-free Tyrode solution containing (in mM): 136 NaCl, 5.4 KCl, 0.33 NaH<sub>2</sub>PO<sub>4</sub>, 1 MgCl<sub>2</sub>, 10 HEPES, 10 dextrose, pH 7.4, maintained at 37°C using a heat exchange coil and water bath. After 3 min of perfusion to flush the coronary vasculature of blood, the solution was switched to Tyrode solution containing 0.1 mg ml<sup>-1</sup> Liberase TH (MilliporeSigma, St Louis, MO, USA) and 15 μM CaCl<sub>2</sub>. The heart was perfused with this enzyme solution for 12 min, removed from the apparatus, and the left ventricular (LV) free wall was dissected and removed. The LV free wall was then cut with a razor into approximately 2 mm<sup>3</sup> pieces and placed into

a 25 ml flask containing warmed enzyme solution diluted 1:1 with Ca<sup>2+</sup>-free Tyrode solution and gently shaken at 37°C for secondary digestion. Following approximately 5 min of shaking, tissue was gently triturated using a flame-polished wide-mouthed Pasteur pipette to liberate cardiomyocytes. The suspension of dissociated cells was collected (while minimizing the collection of undigested tissue chunks) using a serological pipette and filtered through a 140 μm mesh into a 15 ml tube containing Tyrode solution supplemented with 0.2 mM CaCl<sub>2</sub> and 1% BSA. Concurrently, 5 ml of fresh, diluted enzyme solution was added back to the 50 ml flask containing the remaining partially digested tissue and was returned to the heated shaker for another 5 min. The 15 ml tube containing the suspension of dissociated cells was gently centrifuged (20 g, 2 min), the supernatant was removed, and the pellet was resuspended in Tyrode solution containing 0.4 mM CaCl<sub>2</sub>. Cells were allowed to settle by gravity for ~10 min, and then similarly resuspended in 0.6, 0.8 and finally 1.0 mM CaCl<sub>2</sub> Tyrode solution. The above procedure was repeated for each of the cell suspensions collected at 5-min intervals from the secondary digestion, typically a total of 5 times. The fraction(s) with the greatest proportion of healthy myocytes (as estimated by observing shape and striations using phase-contrast light microscopy) were used for experiments. Isolations routinely yielded >75–80% calcium-tolerant rod-shaped cardiomyocytes with clear striations. Cells were stored at room temperature for up to 6 h in 1 mM CaCl<sub>2</sub> Tyrode solution.

### Single cell patch clamp

We recorded membrane currents from isolated left ventricular myocytes using an Axopatch 200B amplifier (Molecular Devices, Sunnyvale, CA, USA) in whole-cell configuration, connected to a computer by a Digidata 1400a A-D converter (Molecular Devices), and controlled by pClamp software (version 10.4; Molecular Devices) at 20–22°C. Patch electrodes were pulled from borosilicate glass (TW150F-3, World Precision Instruments, Sarasota, FL, USA) using a Flaming-Brown horizontal micropipette puller (P-97, Sutter Instruments, Novato, CA, USA). Pipettes had an electrical resistance of 0.75–1.2 MΩ when filled with internal solution containing (in mM): 130 CsCl, 10 NaCl, 0.33 MgCl<sub>2</sub>, 20 tetraethylammonium chloride, 10 HEPES, 0.05 cAMP, 4 MgATP (pH adjusted to 7.2 with CsOH). In experiments measuring the I<sub>Ca,L</sub> response to isoprenaline, cAMP was omitted from the internal solution. For experiments involving simultaneous recording of membrane currents and intracellular Ca<sup>2+</sup> (described below), isolated cardiomyocytes were incubated in 10 μM fluo-4 AM (ThermoFisher Scientific, Waltham, MA, USA) with 0.02% Pluronic F-127 (ThermoFisher) at 20–22°C for 30 min and then allowed to

de-esterify by washing 3 times for 5 min in normal Tyrode solution. Fluo-4 AM-loaded cells were stored in the dark and used up to 2 h following loading. Cells were pipetted into a low volume, laminar flow chamber mounted on an inverted microscope and superfused at a flow rate of 1–2 ml min<sup>-1</sup> with external solution appropriate to each experiment. Cells were first bathed in 1 mM Ca<sup>2+</sup> Tyrode solution. Upon obtaining a gigaseal and low access resistance breakthrough, the bath was rapidly replaced with a solution designed to isolate  $I_{Ca,L}$  containing (in mM): 136 NaCl, 20 CsCl, 1 MgCl<sub>2</sub>, 10 HEPES, 10 dextrose, 1 CaCl<sub>2</sub>, 0.01 tetrodotoxin, pH 7.4. Series resistance was electronically compensated ~ 75%. Cells were held at -80 mV between recordings and  $I_{Ca,L}$  was elicited by applying a 1 s prepulse to -50 mV (to inactivate residual  $I_{Na}$ ), followed by a 200 ms depolarizing step to a test potential of 0 mV. Upon return to -80 mV, SR Ca<sup>2+</sup> load and  $I_{NaCa}$  were simultaneously assessed by applying a 5 s pulse of 10 mM caffeine (in Tyrode solution) to the cell using a rapid perfusion system (Groenke *et al.* 2013).

### Ultra-rapid laser scanning confocal microscopy of subcellular calcium

To record Ca<sup>2+</sup> release from individual couplons evoked by depolarization, we used the ultra-rapid line-scan mode (12  $\mu$ s/line with two-line averaging for an effective temporal resolution of 24  $\mu$ s/line) of the Leica SP5 resonant scanning laser confocal microscope system (Leica Instruments, Wetzlar, Germany) featuring an inverted microscope with a 63 $\times$ /1.2NA water-immersion objective. Image acquisition was synchronized with whole-cell patch clamp depolarization and triggered using digital outputs from the Digidata 1400a. Spatial resolution was 0.19  $\mu$ m/pixel. To reduce photobleaching of the Ca<sup>2+</sup> indicator and to minimize phototoxicity, the laser was shuttered and triggered to open only during the 100 ms acquisition period. All line-scan images, including those described below for field-stimulated and voltage clamp-evoked CaTs, were acquired by placing the scanning line parallel to the long axis of the cell, taking care to avoid intersection with the nucleus. Images of fluo-4 transients were converted to TIFF format and saved to hard disk.

We analysed the ultra-rapid line scan images using custom software (Chantawansri *et al.* 2008) programmed in IDL 6.1 (Harris Geospatial Solutions, Broomfield, CO, USA). Briefly, we identified the exact scan line where the voltage clamp was triggered by the patch clamp amplifier, allowing submillisecond determination of Ca<sup>2+</sup> release latency at each pixel along the scan line. Ca<sup>2+</sup> release site latency (which we refer to as spark latency) was defined as the time interval between triggered depolarization and the earliest time point where fluorescence at a Ca<sup>2+</sup> release

site increased 10% above resting value. We identified individual couplons releasing Ca<sup>2+</sup> by identifying the pixel locations along the scan line where Ca<sup>2+</sup> release from single couplons originated, using a spark location strategy based on the work of Cheng *et al.* (1999), as we described previously (Chantawansri *et al.* 2008). We used the following simplifying assumptions to calculate spark probability ( $P_{\text{spark}}$ ), the probability of Ca<sup>2+</sup> release from individual couplons upon depolarization (Inoue & Bridge, 2003). Couplons are ideally spaced evenly every 1.8  $\mu$ m. Thus, the maximum number of couplons activated along a 180  $\mu$ m line would be 100 (180  $\mu$ m/1.8  $\mu$ m per couplon). If all 100 couplons were activated, we would assign a  $P_{\text{spark}}$  of 1.0. The synchronicity of Ca<sup>2+</sup> release was calculated as the standard deviation of Ca<sup>2+</sup> release latency at all couplons actively releasing Ca<sup>2+</sup> along the scan line ( $\sigma_{\text{spark}}$ ). Local Ca<sup>2+</sup> uptake rates ( $T_{1/2}$ ) were similarly determined at each of these locations (but with conventional line scan speeds, e.g. 2.5 ms per line) by measuring the time in milliseconds for the CaT relaxation to fall 50% from peak to baseline. The variability in Ca<sup>2+</sup> uptake was calculated as the standard deviation of uptake at the locations measured ( $\sigma T_{1/2}$ ).

### Field-stimulated Ca<sup>2+</sup> transients

Cardiomyocytes were loaded with fluo-4 AM as above, or with fura-2 AM (2  $\mu$ M with 0.02% Pluronic F-127 for 15 min at room temperature, followed by three washes of 5 min to allow de-esterification) and placed into a low volume perfusion chamber with platinum field-stimulation electrodes (RC-27, Warner Instruments, Hamden, CT, USA). The bath was perfused at 1–2 ml min<sup>-1</sup>. Cells were excited using a MyoPacer Field Stimulator at 10–30 V, 3 ms pulsewidth (IonOptix, Westwood, MA, USA). Before recording CaTs by line scanning (fluo-4) or ratiometric photometry (fura-2), we paced cells for 10 s to equilibrate SR Ca<sup>2+</sup> content. Evoked CaTs were recorded for 10 s, and the final two CaTs used for analysis. For fura-2 experiments, we used a custom-built system where cells were excited by LED at wavelengths of 360 and 390 nm on a Leica DMI3000B inverted microscope fitted with a 40 $\times$ /1.3NA oil-immersion objective. We used a photomultiplier (IONOPTIX) to measure epifluorescence at 510 nm during alternate excitation (500 Hz) at the above wavelengths. A mask was placed in the light path so epifluorescence from only a well-focused portion of one cell was recorded. We used the  $F_{360}/F_{390}$  ratio (after background subtraction) as a measure of relative changes in free cytosolic Ca. In some experiments, the bath Tyrode solution was then exchanged by perfusion with Tyrode solution containing isoprenaline (ISO, 1  $\mu$ M) and cells were incubated for 3 min, after which CaTs were recorded again as above.

### Simultaneous patch clamp and fluo-4 fluorescence measurements

For some experiments, fluo-4 fluorescence was recorded with a photodiode during simultaneous voltage clamp (as described above) using a custom-designed photometric epifluorescence detection system attached to a Zeiss Axiovert TV100 inverted microscope with a 40×/1.2NA water immersion lens. A 485 nm LED light source was used for excitation and a longpass filter used to restrict emission to >510 nm. Fluorescence was normalized to baseline ( $F/F_0$ ) after background subtraction.

### Baseline correction for diastolic calcium

To correct for increased baseline fluo-4 fluorescence in HFrEF and HFpEF compared to control (consistent with elevated diastolic  $Ca^{2+}$  as found in the fura-2 experiments described in Results), we employed the following correction ( $F/F_{0c}$ ):

$$F/F_{0c} = (F/F_0) \times (R_{\text{dias model}}/R_{\text{dias control}}),$$

where  $F/F_{0c}$  is the corrected fluo-4 fluorescence and  $R_{\text{dias model}}/R_{\text{dias control}}$  was the measured ratio of fura-2 diastolic fluorescence in either the HFrEF model or the HFpEF model compared to the control model. The ratios used were 1.125 for HFrEF and 1.25 for HFpEF.

### Protein isolation, electrophoresis and immunoblotting

Tissue was homogenized in RIPA buffer (Thermo Fisher) using twice the manufacturer-recommended amounts of protease and phosphatase inhibitor cocktails (Halt, Thermo Fisher). Protein quantification was performed by Pierce BCA protein assay (Thermo Fisher). Electrophoresis was performed using NuPage protein gels of 4–12%. Proteins were transferred to PVDF membranes using a Trans-Blot Turbo transfer system (BioRad). Membranes were blocked for 1 h in tris-buffered saline + 0.1% Tween-20 (TBS-T) solution containing 5% bovine serum albumin. Antibodies used were Cav1.2 (Alomone ACC-003, 1:600), pSer1928 Cav1.2 (Badrilla, A010-70 1:1000), SERCA2 (Invitrogen, MA3-919, 1:1000), PLN (ThermoFisher, PA5 78410, 1:1000), pThr17 PLN (Badrilla, A010-13AP, 1:1000), pSer16 PLN (Badrilla, A010-12AP, 1:5000), NCX (R3F1 (Porzig *et al.* 1993) 1:500) and glyceraldehyde 3-phosphate dehydrogenase (GAPDH) (3683S, Cell Signalling, 1:3000). Immunoreactivity was detected by enhanced chemiluminescence (SuperSignal West Pico Plus, Thermo Fisher) using a ChemiDoc Imager (BioRad).

### Immunoprecipitation

Tissue was homogenized in homogenization buffer containing (in mM): HEPES 20, NaCl 150, EDTA 5, KF 25, sodium orthovanadate 1 with glycerol 20%, triton X-100 0.5% and protease inhibitor cocktail (Roche, cOmplete), pH 6.8. Anti-RyR antibody (Abcam, ab2868) was incubated with Dynabeads Protein G (Invitrogen) for 40 min at room temperature (1  $\mu$ l antibody + 11  $\mu$ l beads per sample). The beads were washed with PBS-0.05% Tween-20 twice and homogenization buffer once. A 400  $\mu$ l aliquot of lysate (total protein concentration of 1 mg ml<sup>-1</sup>) was incubated at 4°C overnight with antibody-bead in homogenization buffer. After washing, electrophoresis was performed using protein gels of 8%. Proteins were transferred to PVDF membranes using the Trans-Blot semi-dry transfer system (BioRad). Membranes were blocked for 1 h in PBS-0.05% Tween-20 solution containing 5% dried skimmed milk. Antibodies used were RyR2 (Abcam, ab2868, 1:5000) and pSer2808 RyR2 (Badrilla, A010-30AP, 1:1000). Data were normalized to RyR in the immunoprecipitated sample.

### Reverse transcription quantitative polymerase chain reaction

Following isolation and reacclimating to 1 mM  $Ca^{2+}$  in Tyrode solution, cardiomyocytes were pelleted by centrifugation and flash frozen. Total RNA was isolated from myocyte samples using Rneasy Mini Kit (Qiagen). RNA quality was determined using a spectrophotometer and was reverse transcribed using a cDNA conversion kit from 2  $\mu$ g RNA with the High Capacity RNA-to-cDNA Kit (Applied Biosystems). cDNA in combination with RT<sup>2</sup> SYBR Green qPCR Mastermix (Cat. No. 330529) was used with RT2 qPCR Assays. Primers were designed to detect target transcripts as follows:

GAPDH (AF106860.2), 5'-AGTTCAACGGCACAGTCA-AG-3' (forward), 5'-TACTCAGCACCAGCA TCACC-3' (reverse)

rat a2d3 (NM\_175595), 5'-TCCGAACGCACCATCAA-G-3' (forward), 5'-ACTGTCCACCACCACCAT-3' (reverse)

rat a2d2 (NM\_175592), 5'-CAGTGGTGGGTGT-CAAAC-3' (forward), 5'-TACCTCGCAGTCCATCTC-3' (reverse)

rat a2d1 (NM\_012919), 5'-AGCCTATGTGCCATCAATT-AC-3' (forward), 5'-AGTCATCCTCTTCCATT TCAAC-3' (reverse)

CaVB1 (NM\_017346.1), 5'-GCGAGCACCTGGCG-GAGTAC-3' (forward), 5'-GCGGTAGCCATGGTG CCGTT-3' (reverse)

CaVB2 (NM\_053851.1), 5'-AGTGGGACAGGTCG-AGGCCT-3' (forward), 5'-CACGGTGTGGAACA TAGCGGTC-3' (reverse)  
 CaVB3 (NM\_012828.2), 5'-TTCACCCCTGGAGC-GGGACA-3' (forward), 5'-ACGGTGAGGCTGG TACAGGTC-3' (reverse)  
 CaVB4 (NM\_012828.2), 5'-ACCTGGAGGCATATT-GGCGTGC-3' (forward), 5'-TGGTTGCTATGCCT CATCCGCT-3' (reverse)  
 CaVB2 splice variants:  
 CaVB2a: 5'-ATGCAGTGCTGCGGGCTGGTAC-3' (forward)  
 CaVB2b: 5'-ATGCTTGACAGGCAGTTGGTG-3' (forward)  
 CaVB2c: 5'-ATGGACCAGGCGAGTGGACTGG-3' (forward)  
 CaVB2d: 5'-AAAGCGCGGCTCCCG-3' (forward)  
 Common CaVB2 antisense primer: 5'-TCCCGTCTCTTCCAAAGACA-3' (forward)

CT values were exported to an Excel file to create a table of CT values. This table was then uploaded on to the data analysis web portal at <http://www.qiagen.com/geneglobe>. Each cycle threshold (CT) value was normalized to the CT value of GAPDH. Fold change was calculated with  $2^{-(\Delta\Delta CT)}$  compared with the control group. The *P* values were calculated based on a Student's *t* test of the replicate  $2^{-(\Delta CT)}$  values for each gene in the control group and HFpEF groups.

## Statistics

Data are expressed as means  $\pm$  SD. Statistical analysis was performed using Prism 8.0 (GraphPad Software, Inc.; La Jolla, CA, USA) or Microsoft Excel. The Shapiro-Wilk statistic was used to test for normality. One-way ANOVA with Holm-Sidak *post hoc* correction for multiple comparisons was used for statistical comparison of measures among three groups (control, HFrEF, HFpEF). Two-way ANOVA with Holm-Sidak *post hoc* correction for multiple comparisons was used when appropriate. For measures comparing only HFpEF to control, Student's unpaired or paired two-tailed *t* test (normal distribution) or Mann-Whitney rank test (non-normal distribution) was used to compare group means. *P* < 0.05 was considered statistically significant.

## Results

### Echocardiographic and morphometric assessment of HFrEF and HFpEF

As we have shown previously using invasive haemodynamic monitoring and echocardiography, when compared to DS rats fed low-salt diets (control),

DS rats fed high salt develop profound hypertension (mean blood pressure  $238 \pm 16/175 \pm 31$  mmHg; *N* = 10; *P* < 0.0001 vs. control; Fig. 1B) and posterior wall thickening (in mm: HFpEF  $2.4 \pm 0.33$  (*N* = 30) vs. control  $1.9 \pm 0.32$  (*N* = 32), *P* < 0.0001; Fig. 1C), ultimately exhibiting the cardinal haemodynamic and clinical features of human HFpEF (Ogihara *et al.* 2002; Gallet *et al.* 2016; Cho *et al.* 2017). Notably, systolic function is preserved (EF > 65%, Fig. 1D and H), diastolic function is impaired (reduced E/A ratio and increased E/e' ratio; Fig. 1E, F and I), with objective signs of heart failure: pulmonary congestion as manifested by increased lung to body weight ratio (HFpEF  $4.9 \pm 0.5$  (*N* = 27) vs. control  $3.8 \pm 0.3$  (*N* = 22); *P* < 0.0001) and increased left atrial size (Fig. 1G), consistent with adaptation to elevated ventricular filling pressure. We also found increased LV mass by echo (HFpEF  $1154 \pm 204$  mg (*N* = 17) vs. control  $855 \pm 138$  mg (*N* = 29); *P* < 0.001) as well as increased single myocyte capacitance (HFpEF  $317 \pm 70$  pF (*N* = 29) vs. control  $250 \pm 45$  pF (*N* = 17); *P* < 0.002), indicative of hypertrophy. Other features of this model, including the high mortality (~50%), are summarized in our previous study (Cho *et al.* 2017).

To investigate HFrEF, we created a left anterior descending artery (LAD) coronary ligation model and used pre-infarct SD or age-matched low-salt DS rats as controls. Six to eight weeks following LAD ligation, SD rats developed HFrEF characterized by reduced ejection fraction (EF; HFrEF  $42.9 \pm 9.5\%$  (*N* = 6) vs. sham  $72.0 \pm 1.1\%$  (*N* = 6); *P* < 0.0001) as described previously (Pfeffer *et al.* 1979; Wang *et al.* 2016; Fig. 1D and H). HFrEF rats also showed evidence of elevated filling pressures with increased left atrial diameter (Fig. 1G), and pulmonary congestion with increased lung/body weight ratio (HFrEF  $3.83 \pm 0.22$  mg g<sup>-1</sup> (*N* = 4) vs. sham  $3.42 \pm 0.11$  mg g<sup>-1</sup> (*N* = 4); *P* < 0.02) and increased LV mass (HFrEF  $1054 \pm 62$  (*N* = 6) vs. sham  $777 \pm 197$  (*N* = 6); *P* < 0.020). Cell capacitance was not significantly increased in HFrEF (control  $244 \pm 65$  pF (*N* = 25); HFrEF  $271 \pm 72$  pF (*N* = 31); *p* > 0.05 (NS)).

### Excitation-contraction coupling is impaired in HFrEF but enhanced in HFpEF

To probe EC coupling, we recorded CaTs at 1 Hz using the ratiometric Ca<sup>2+</sup> indicator fura-2 in single ventricular cardiomyocytes isolated from control, HFrEF and HFpEF animals. As is evident in representative signals (Fig. 2A), CaT amplitude was reduced in HFrEF myocytes ( $\Delta F_{360}/F_{390} = 0.92 \pm 0.41$ ; *P* < 0.05), but increased in HFpEF ( $\Delta F_{360}/F_{390} = 1.71 \pm 0.53$ ; *P* < 0.001) versus control ( $\Delta F_{360}/F_{390} = 1.21 \pm 0.46$ ) (Fig. 2B). While diastolic Ca<sup>2+</sup> was higher than control in both HF models ( $F_{360}/F_{390}$ : control  $2.18 \pm 0.53$ ; HFrEF  $2.45 \pm 0.49$ , *P* < 0.05;

HFpEF  $2.72 \pm 0.52$ ,  $P < 0.001$ ) (Fig. 2C), systolic  $\text{Ca}^{2+}$  was increased only in HFpEF ( $F_{360}/F_{390}$ : control  $3.38 \pm 0.80$  vs. HFpEF  $4.43 \pm 0.78$ ,  $P < 0.001$ ) (Fig. 2D). In fluo-4 loaded HFpEF cells, increased pacing frequency did not cause further increase in diastolic  $\text{Ca}^{2+}$  (Fig. 7C).

Further dissection using simultaneous patch clamp and fluo-4 fluorescence photometry (Fig. 3A) revealed unchanged L-type  $\text{Ca}^{2+}$  current ( $I_{\text{Ca,L}}$ ; Fig. 3B) and sarcoplasmic reticulum (SR)  $\text{Ca}^{2+}$  load as assessed by caffeine (Fig. 3E) in HFrEF cells. NCX current in response to caffeine was modestly increased ( $\text{pA pF}^{-1}$ : control  $-0.91 \pm 0.33$  ( $N = 27$ ); HFrEF  $-1.05 \pm 0.21$  ( $N = 52$ );  $P < 0.05$ ). However, EC coupling gain (expressed as amplitude of the CaT ( $\Delta F/F_{0c}$ ) divided by the peak amplitude of the eliciting  $\text{Ca}^{2+}$  current ( $I_{\text{Ca,L}}$ ) at 0 mV ( $\text{pA pF}^{-1}$ )) was reduced in HFrEF (control  $-0.71 \pm 0.28$ ; HFrEF  $-0.46 \pm 0.22$ ;  $P < 0.05$ ), a hallmark of defective EC coupling (Fig. 3D).

In contrast,  $I_{\text{Ca,L}}$  (Fig. 3B) was increased in HFpEF ( $\text{pA pF}^{-1}$ : control  $-7.77 \pm 2.11$ ; HFpEF  $-9.61 \pm 2.09$ ;  $P < 0.02$ ) but without a significant change in EC coupling gain (Fig. 3D), SR  $\text{Ca}^{2+}$  content (Fig. 3E), or NCX current in response to caffeine ( $\text{pA pF}^{-1}$ : control  $-1.03 \pm 0.46$  ( $N = 9$ ); HFpEF  $-1.04 \pm 0.29$  ( $N = 17$ ),  $p > 0.05$  (NS)).  $\text{Ca}_v1.2$  expression, but not phosphorylation, was enhanced in HFpEF (Fig. 8A,  $P < 0.05$ ). The lack of phosphorylation differs from HFrEF (Bryant *et al.* 2015), consistent with the observed differences in  $I_{\text{Ca,L}}$ . qPCR showed no significant changes in the abundance of  $\text{Ca}_v1.2$ -interacting subunit transcripts (Table 1). Thus, in HFpEF, an increase in  $I_{\text{Ca,L}}$  due to enhanced protein expression (with an increase in the number of L-type  $\text{Ca}^{2+}$  channels per couplon) could account for the increased CaT amplitude, while in HFrEF, impaired coupling between  $\text{Ca}^{2+}$  entry and  $\text{Ca}^{2+}$  release

must be invoked (given preserved  $I_{\text{Ca,L}}$  and SR  $\text{Ca}^{2+}$  load) to account for the decrease in CaTs, echoing the conclusions of extensive previous work on HFrEF myocytes (Gomez *et al.* 2001; Zima *et al.* 2014).

### Calcium spark recruitment is compromised in HFrEF but not in HFpEF

Ultra-fast laser scanning confocal microscopy can be used to record microscopic aspects of EC coupling and local Ca-induced  $\text{Ca}^{2+}$  release (CICR) including probability of  $\text{Ca}^{2+}$  release from individual couplons (spark probability ( $P_{\text{spark}}$ )), synchronicity of  $\text{Ca}^{2+}$  release from all couplons along the scan line (spark variance ( $\sigma_{\text{spark}}$ )), and latency of  $\text{Ca}^{2+}$  release (spark latency) in response to triggering by  $I_{\text{Ca,L}}$  (Inoue & Bridge, 2003; Chantawansri *et al.* 2008). These values allow quantification of subcellular changes in couplon recruitment that might rationalize differences in EC coupling efficiency between HFrEF and HFpEF. In patch-clamped HFrEF myocytes (Fig. 4),  $P_{\text{spark}}$  was lower than control ( $P_{\text{spark}}$ : control  $0.63 \pm 0.10$  ( $N = 26$ ) vs. HFrEF  $0.48 \pm 0.06$  ( $N = 9$ );  $P < 0.001$ , Fig. 4C), with fewer couplons along the scan line releasing  $\text{Ca}^{2+}$  upon triggering by a voltage clamp to 0 mV, despite unchanged  $I_{\text{Ca,L}}$  and SR  $\text{Ca}^{2+}$  load. Furthermore, the timing of  $\text{Ca}^{2+}$  release at each couplon along the scan line was highly dyssynchronous in HFrEF when expressed as variance ( $\sigma_{\text{spark}}$  in ms: HFrEF  $1.68 \pm 0.36$  ( $N = 13$ ) vs. control  $1.28 \pm 0.38$  ( $N = 14$ );  $P < 0.001$ ; Fig. 4D), similar to prior descriptions (Litwin *et al.* 2000; Chantawansri *et al.* 2008; Heinzel *et al.* 2008). In contrast, two-thirds of the couplons along the scan line in HFpEF released  $\text{Ca}^{2+}$  in response to  $I_{\text{Ca}}$  (i.e.  $P_{\text{spark}} = 0.66 \pm 0.10$ ) with high synchronicity

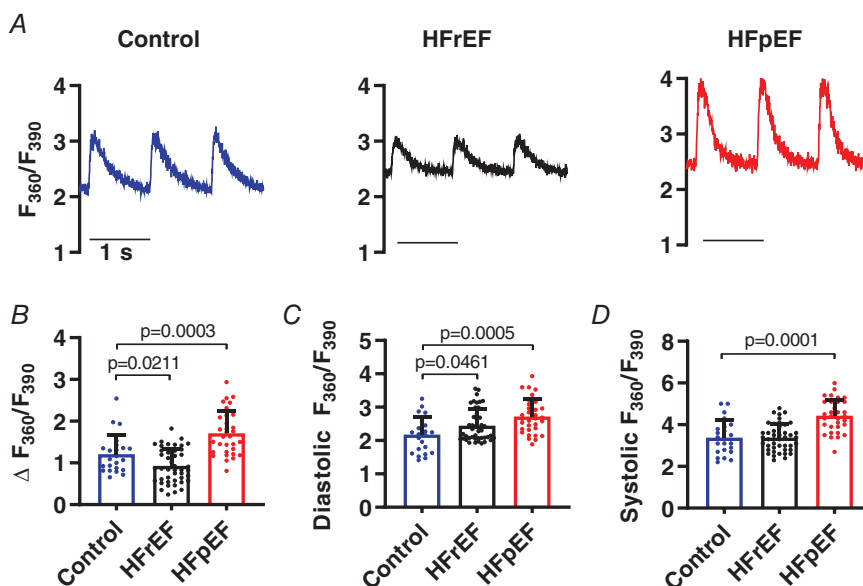


**Figure 2. Calcium transients are reduced in HFrEF but enhanced in HFpEF** A, representative fura-2  $\text{Ca}^{2+}$  transients ( $F_{360}/F_{390}$ ) elicited by field stimulation at 1 Hz in cardiomyocytes isolated from control, HFrEF and HFpEF animals. B–D, pooled data analysing the amplitude ( $\Delta$ ), diastolic and systolic fura-2 ratios ( $n = 23$ , 44 and 32 cells from 3 control, 5 HFrEF and 5 HFpEF rats). Results are shown as means  $\pm$  SD. Statistics are calculated by one-way ANOVA. [Colour figure can be viewed at [wileyonlinelibrary.com](http://wileyonlinelibrary.com)]

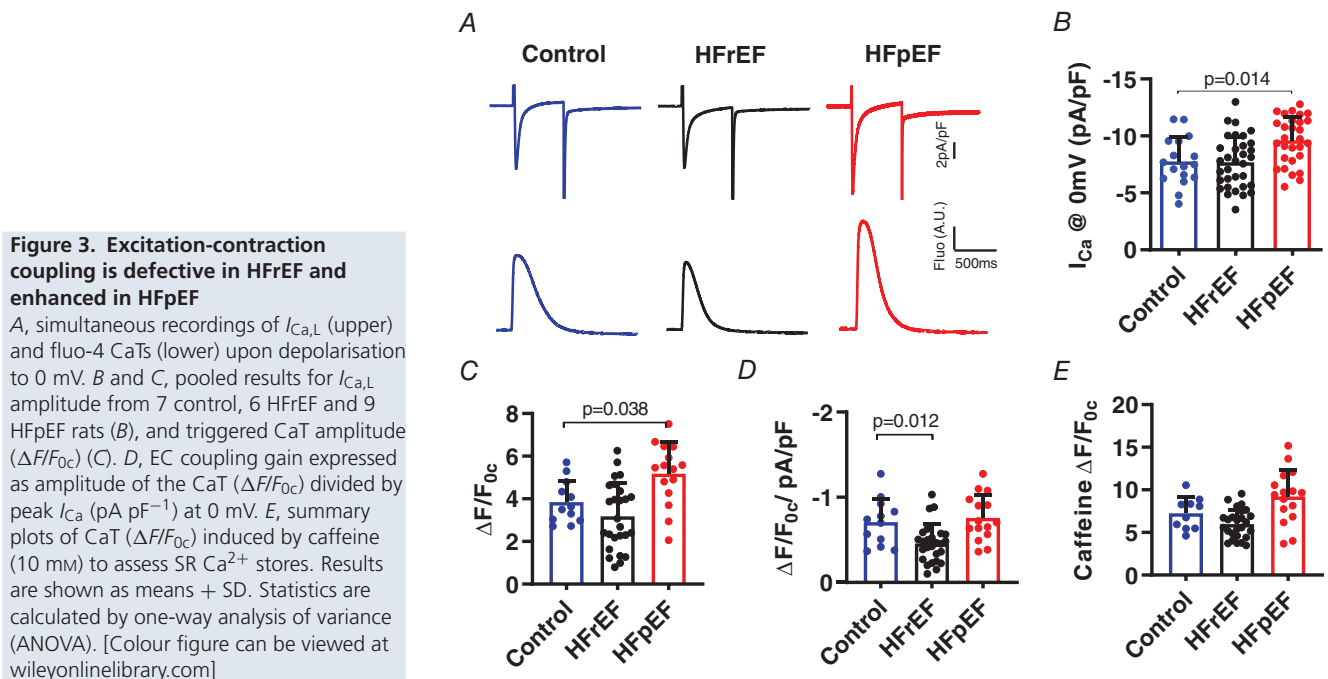
**Table 1. PCR analysis of LTCC-interacting subunits**

	AVG Ct		$\Delta$ Ct vs. GAPDH		Standard deviation		Fold change	95% CI	P value
	Control	HFpEF	Control	HFpEF	Control	HFpEF			
GAPDH	16.49	16.24	0	0	0	0	1	(1.00, 1.00)	0
a2D-3	33.73	32.3	17.238	16.053	0.679	2.414	2.272	(0.00001, 5.57)	0.326
a2D-2	24.33	24	7.839	7.755	0.535	1.575	1.060	(0.41, 1.71)	0.893
a2D-1	24.27	23.56	7.778	7.321	1.089	1.936	1.373	(0.81, 1.94)	0.148
CaVB2d	25.92	25.41	9.426	9.162	0.685	1.346	1.200	(0.60, 1.80)	0.331
CaVB2c	28.66	28.18	12.172	11.936	0.854	1.442	1.178	(0.69, 1.66)	0.328
CaVB2b	22.36	21.98	5.868	5.738	0.519	1.520	1.094	(0.44, 1.75)	0.903
CaVB2a	35	35	18.509	18.756	0.000	0.000	0.843	(0.00001, 1.74)	0.946
CaVB4	32.46	31.91	15.970	15.664	1.691	1.784	1.237	(0.00001, 3.27)	0.384
CaVB3	26.54	25.36	10.051	9.117	1.799	1.085	1.911	(0.00001, 4.45)	0.406
CaVB2	26.11	26.14	9.618	9.896	1.615	1.488	0.825	(0.26, 1.39)	0.454
CaVB1	31.16	30.06	14.670	13.820	0.973	1.181	1.802	(0.61, 2.99)	0.102

( $\sigma_{\text{spark}} = 0.88 \pm 0.17$  ms) compared to HFrEF ( $P < 0.001$  vs. HFpEF) (Fig. 3B–D). Likewise,  $\text{Ca}^{2+}$  release latency (i.e. the time from depolarization to  $\text{Ca}^{2+}$  release) was shorter in HFpEF ( $5.42 \pm 0.63$  ms) than HFrEF ( $7.19 \pm 1.42$  ms,  $P < 0.001$  vs. HFpEF) (Fig. 4B and E), consistent with more effective ryanodine receptor (RyR) recruitment by  $I_{\text{Ca}}$  in HFpEF myocytes. These results pinpoint fundamental differences in the behaviour and interaction of L-type  $\text{Ca}^{2+}$  channels (LCCs) and RyRs in HFpEF versus HFrEF.

The EC coupling machinery is concentrated within the transverse-axial tubule (TAT) system (Kockskamper *et al.* 2001; Yue *et al.* 2017), which is disorganized

and depleted in HFrEF (Louch *et al.* 2006; Song *et al.* 2006). Conversely, little is known about remodelling of the TAT system in HFpEF, although it is reportedly intact in human HFpEF tissue (Frisk *et al.* 2018). In freshly isolated cardiomyocytes, TAT architecture (visualized with Di-4 Anepps (Fig. 5A) and quantified as previously described (Guo & Song, 2014)) was overtly disrupted in HFrEF ( $\text{TT}_{\text{density}} = 3.73 \pm 1.01\%$  in HFrEF vs.  $5.90 \pm 0.85\%$  in control;  $P < 0.001$ ; Fig. 5B;  $\text{TT}_{\text{integrity}} = 1.65 \pm 0.52$  in HFrEF vs.  $2.59 \pm 0.69$  in control;  $P < 0.001$ ; Fig. 5C), but remained well-organized in HFpEF ( $\text{TT}_{\text{density}} = 5.60 \pm 0.80\%$ ;  $\text{TT}_{\text{integrity}} = 2.63 \pm 0.82$ ;



both  $p > 0.05$  (NS) vs. control; Fig. 5B and C). Axial tubule density was similar between groups (Fig. 5D). Loss of t-tubule integrity probably contributes to spark dyssynchrony in HFrEF, while preserved TAT architecture supports effective spark recruitment in HFpEF by enabling direct engagement of  $\text{Ca}^{2+}$  release channels by  $\text{Ca}^{2+}$  entering the dyadic cleft through LCCs.

### $\beta$ -Adrenergic responses of $I_{\text{Ca}}$ , $\text{Ca}^{2+}$ transients, contractility and relaxation are impaired in HFpEF

Given that EC coupling abnormalities in HFrEF are well understood, and our findings there largely confirmatory, we focus more exclusively on HFpEF as we continue. Symptoms in HFpEF patients are most evident upon exertion (Borlaug *et al.* 2010), reflecting reduced inotropic

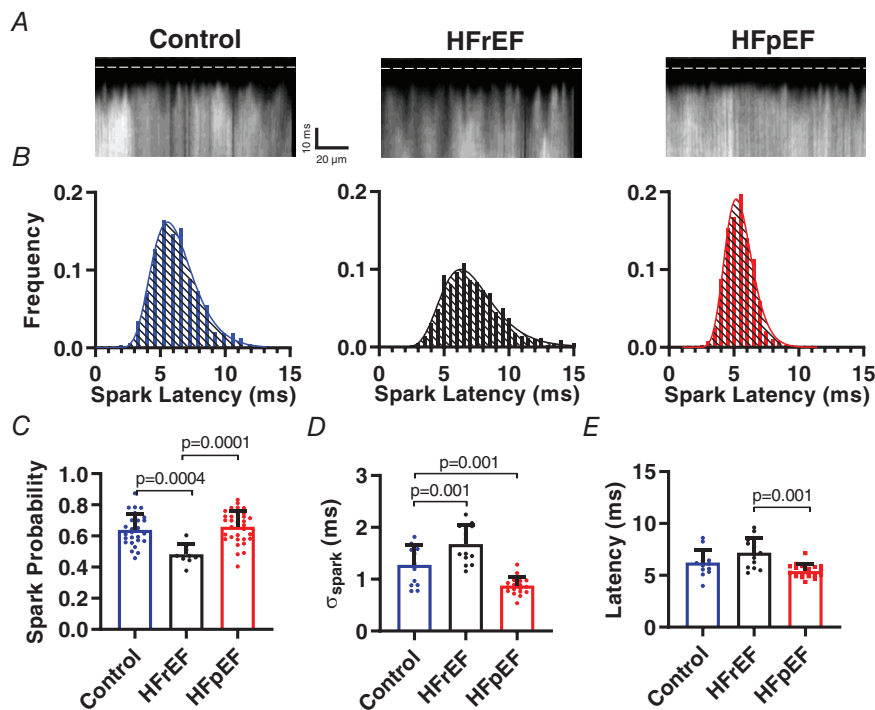


**Figure 4. Microscopic EC coupling is compromised in HFrEF but enhanced in HFpEF**

A, individual  $\text{Ca}^{2+}$  sparks triggered by depolarisation to 0 mV resolved using ultra-high-speed resonant confocal line scanning in fluo-4-loaded patch-clamped cardiomyocytes. Dashed line indicates onset of depolarisation. B, histograms of spark latencies in control (blue), HFrEF (black) and HFpEF (red). C–E, mean ( $\pm$  SD) spark probability, spark latency variability (plotted as standard deviation of latency), and spark latency ( $n = 13, 14$  and  $19$  cells from 6, 3 and 5 control, HFrEF and HFpEF rats, respectively). Statistics are calculated by one-way ANOVA. [Colour figure can be viewed at [wileyonlinelibrary.com](http://wileyonlinelibrary.com)]

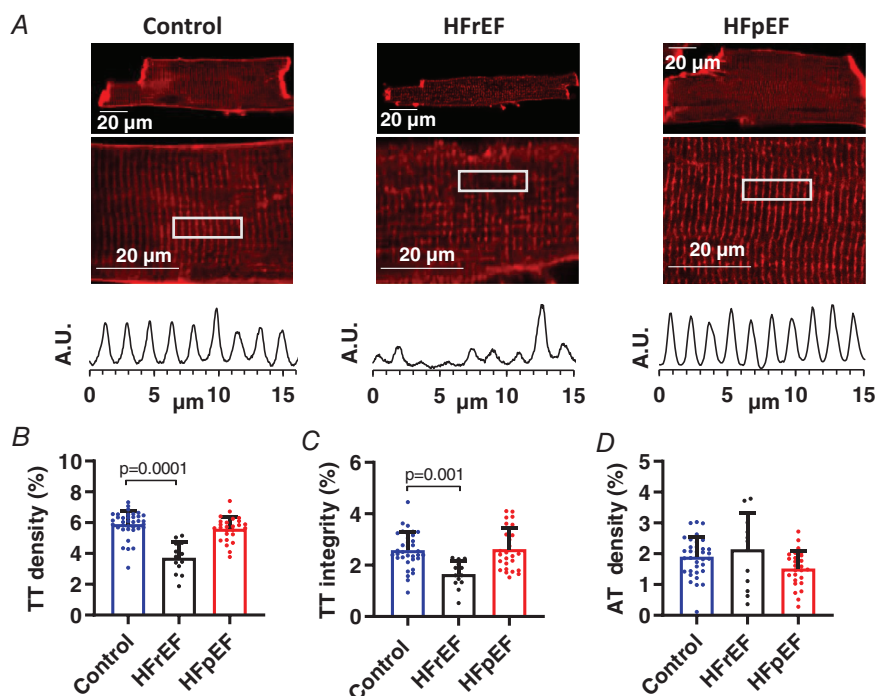


**Figure 5. Transverse-tubules are depleted in HFrEF but intact in HFpEF**

A, representative t-tubule staining with Di-4-ANEPPS (upper) and intensity profiles (lower) assessing t-tubule regularity in the regions outlined by white box. B–D, mean ( $\pm$  SD) t-tubule (TT) density, t-tubule (TT) integrity and axial tubule (AT) density in Di-4-ANEPPS-loaded cells ( $n = 36, 13$  and  $26$  cells from three, two and four control, HFrEF and HFpEF animals, respectively). Statistics are calculated by one-way analysis of variance (ANOVA). [Colour figure can be viewed at [wileyonlinelibrary.com](http://wileyonlinelibrary.com)]

and lusitropic reserves (Norman *et al.* 2011). The  $\beta$ -agonist isoprenaline (ISO) activates protein kinase A (PKA) signalling and, through downstream phosphorylation of key EC coupling proteins, increases contractility and accelerates relaxation. We found that while including ISO (1  $\mu$ M) in the bath solution increased  $I_{Ca,L}$  (at 0 mV) in control cells by 96%, it was much less effective in HFpEF, increasing  $I_{Ca,L}$  (which has a greater amplitude at baseline compared to control) by only 38% ( $P < 0.001$ ; Fig. 6A and B). Similarly, ISO-induced increases in CaT amplitude and decay kinetics were severely blunted in HFpEF myocytes compared to control (Fig. 6C–F), without further elevating diastolic  $Ca^{2+}$  (data not shown). Thus, key aspects of EC coupling in HFpEF myocytes are resistant to  $\beta$ -stimulation, with potential implications for both systolic and diastolic function in HFpEF during exercise.

Abnormal relaxation is a key characteristic of HFpEF hearts. Speculation (Loffredo *et al.* 2014), yet untested in a phenotype-verified model, posits that reduced or defective SR  $Ca^{2+}$  reuptake contributes to impaired relaxation in HFpEF. Although our HFpEF rat model exhibits profound diastolic dysfunction (Fig. 1E, F and I; see also Gallet *et al.* 2016), CaT decay was comparable in control and HFpEF cells at baseline (CaT  $T_{1/2} = 352 \pm 158$  ms in control vs.  $332 \pm 124$  ms in HFpEF,  $p > 0.05$  (NS); Fig. 6F). Only upon closer examination using confocal imaging (Fig. 7A) did we observe significant subcellular spatiotemporal inhomogeneities of  $Ca^{2+}$  uptake in HFpEF

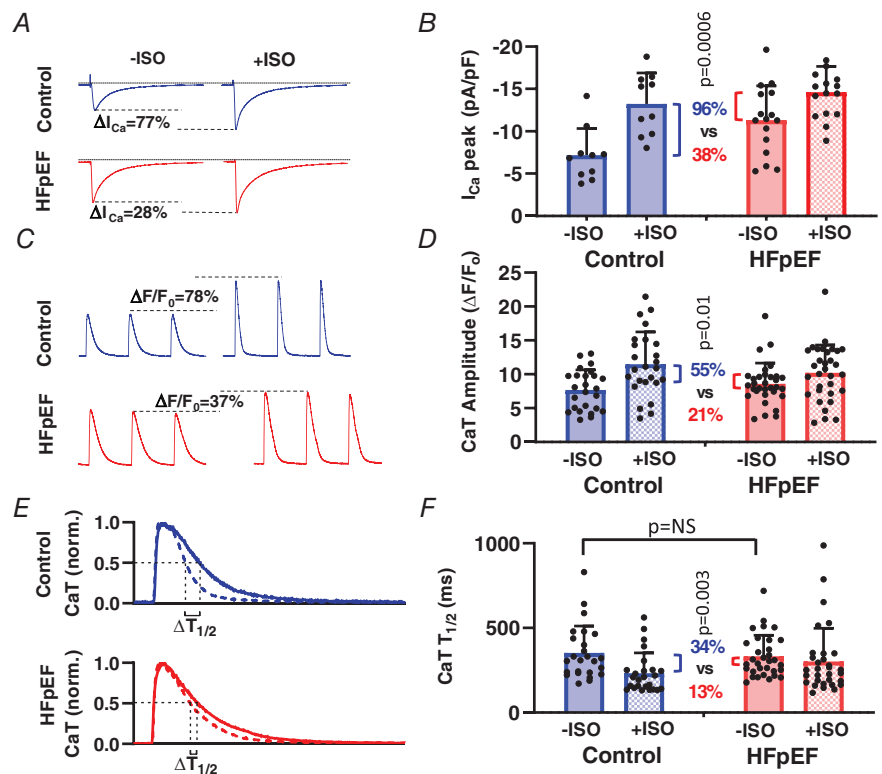
( $\sigma T_{1/2} = 69.9 \pm 21.5$  ms) compared to control cells ( $\sigma T_{1/2} = 42.3 \pm 13.4$  ms;  $P < 0.01$ ) (Fig. 7B). In other disease models, notably HFrEF, high local variability in  $Ca^{2+}$  uptake has been associated with abnormal relaxation and arrhythmia (Hohendanner *et al.* 2013).

Except for an increase in phospholamban (PLN), we found no significant changes in expression of the major proteins responsible for removal of cytosolic  $Ca^{2+}$ , namely the sarcoplasmic/endoplasmic reticulum  $Ca^{2+}$  ATPase (SERCA), and the sodium-calcium exchanger (NCX) (Fig. 8A). Likewise, there was no significant increase in phosphorylation of PLN at either the Ser16 or Thr17 phosphorylation sites (Fig. 8B). These findings contrast with the literature in HFrEF, where reduced SERCA expression and hypophosphorylation of PLN are well documented (Eisner *et al.* 2013; Marks, 2013; Hulot *et al.* 2017). We did find a significant increase in RyR phosphorylation Ser2808 in HFpEF (Fig. 8C), which is also reported in HFrEF (Wehrens *et al.* 2006), but this was not associated with depletion of SR  $Ca^{2+}$  (Fig. 3E). Thus, post-translational regulation, not expression, of EC coupling proteins appears to be responsible for the blunted  $\beta$ -adrenergic response in HFpEF rat myocytes.

### Discussion

While both HFrEF and HFpEF patients have the clinical syndrome of heart failure, key differences in

**Figure 6. Impaired  $\beta$ -adrenergic response of  $I_{Ca,L}$  and  $Ca^{2+}$  transient kinetics in HFpEF**  
 A and B, representative (A) and mean + SD  $I_{Ca,L}$  (B) upon depolarisation to 0 mV, at baseline (–ISO) and after isoprenaline (+ISO), in 10 cells from three control rats and 16 cells from three HFpEF rats. C and D, representative (C) and mean CaT amplitudes (D) elicited by field stimulation before (–ISO) and after (+ISO) isoprenaline in 25 cells from 4 control rats and 32 cells from 5 HFpEF rats. E, normalized CaT before (continuous line) and after (dashed line) ISO indicating measurement of CaT relaxation half-time ( $T_{1/2}$ ). F, mean (+ SD)  $Ca^{2+}$  uptake rate ( $T_{1/2}$ ) before and after ISO in 25 cells from 4 control rats and 32 cells from 5 HFpEF rats. Statistics are calculated using paired Student's *t* test to compare the effect of ISO on relative change in  $I_{Ca}$ , CaT amplitude and CaT  $T_{1/2}$ , as shown by the colour-coded percentage changes accompanied by *P* values. [Colour figure can be viewed at [wileyonlinelibrary.com](http://wileyonlinelibrary.com)]



cardiac function point to distinct underlying pathological mechanisms. Defective EC coupling is a central feature of HFrEF, and mechanistically links cellular pathophysiological and cytoarchitectural changes to organ level systolic dysfunction. We find that HFpEF differs qualitatively from HFrEF in terms of  $\text{Ca}^{2+}$  cycling. That conclusion is based on investigations of EC coupling in the DS rat model of HFpEF, which exhibits the major haemodynamic and clinical features of the human syndrome, including hypertension, diastolic dysfunction, pulmonary congestion, cachexia, lethargy and exercise intolerance (Guazzi *et al.* 2001; Gallet *et al.* 2016; Cho *et al.* 2018b; Pieske *et al.* 2019), and relevant co-morbidities such as insulin resistance (Ogihara *et al.* 2002). In stark contrast to the defective CICR mechanism that typifies HFrEF, EC coupling is actually *enhanced* at baseline in HFpEF rats, with increased  $I_{\text{Ca}}$ , increased CaT amplitude, a high probability of couplon recruitment ( $P_{\text{spark}}$ ), improved  $\text{Ca}^{2+}$  release synchrony (decreased  $\sigma_{\text{spark}}$ ) and shorter  $\text{Ca}^{2+}$  release latency compared to control rats. These physiological enhancements in EC coupling, the *opposite* of changes in HFrEF, are likely to be adaptations that allow the heart to maintain effective contractile function in the face of increased ventricular wall stiffness produced by the known increased collagen deposition/fibrosis of this model (Gallet *et al.* 2016) and possibly titin hypophosphorylation (Hamdani *et al.* 2013), a factor underlying diastolic dysfunction in other rat models of HFpEF.

For EC coupling to occur with high fidelity, two things are required. First, LCCs and RyRs must maintain close proximity. The ordered network of t-tubules ensures this juxtaposition by placing sarcolemmal LCCs a short distance away (across the diadic cleft) from RyRs on the junctional SR. Second, a sufficient number of LCCs in

each couplon must open with a high enough probability, open time and short enough latency to trigger RyRs synchronously (Inoue & Bridge, 2003). Reduced  $\text{Ca}^{2+}$  spark probability and synchrony have been identified in post-infarct HFrEF in rabbit (Litwin *et al.* 2000) as well as a metabolic stress model of ischaemia featuring reduced LCC open probability, increased latency and shorter open times (Chantawansri *et al.* 2008). Disruption of t-tubules in HFrEF has been directly associated with the systolic impairments characteristic of the disease, including reduced efficiency and synchrony of CICR (Louch *et al.* 2006; Heinzel *et al.* 2008; Frisk *et al.* 2016; Hong & Shaw, 2017). As t-tubules remodel, the spatially dependent communication between LCCs and RYRs is disrupted (Song *et al.* 2006). This produces a pool of 'orphaned' RyRs, which exhibit delayed  $\text{Ca}^{2+}$  release, while their hyperphosphorylation in HF contributes to SR leakiness and reductions in SR  $\text{Ca}^{2+}$  content. In sum, these factors, including t-tubule disruption (Fig. 5), contribute prominently to the impaired EC coupling we observe in HFrEF and probably contribute to reduced contractility (Fig. 1D and H).

In marked contrast, HFpEF rats exhibit an enhanced CICR mechanism *versus* HFrEF, characterized by increased  $I_{\text{Ca}}$ , high  $P_{\text{spark}}$  featuring high release synchronicity, and short  $\text{Ca}^{2+}$  release site latency, yielding increased CaT amplitude. This high efficiency EC coupling could be helpful in overcoming the fibrosis-induced stiffness associated with HFpEF (Gallet *et al.* 2016), but also predicts a lack of contractile reserve, as described in humans (Borlaug *et al.* 2010). The increased CaT with insignificant increase in SR  $\text{Ca}^{2+}$  also suggests an increase in fractional release of SR Ca. Since the t-tubule network in HFpEF appears similar to control, the enhanced CICR

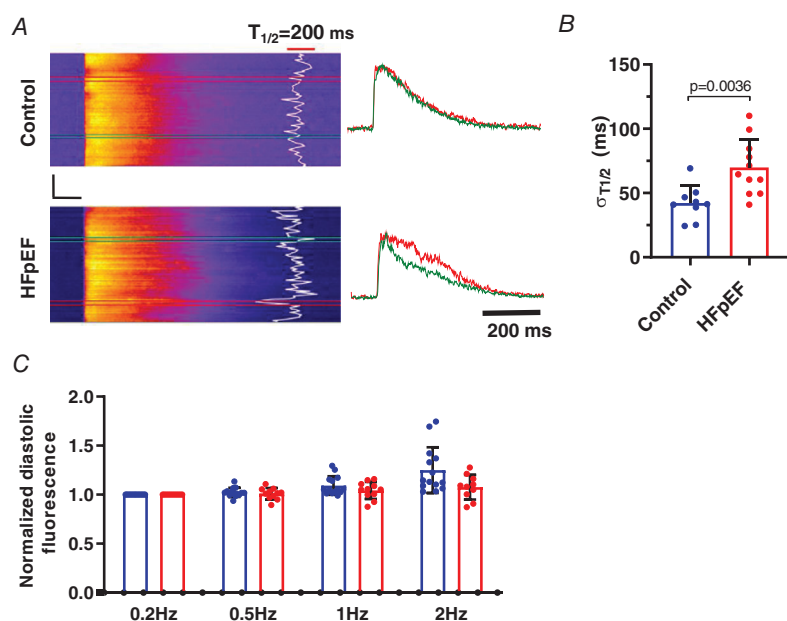


**Figure 7. Defective local uptake of calcium in HFpEF cells**

A, representative confocal line scan (2.5 ms/line) CaTs elicited by field stimulation in cardiomyocytes isolated from control and HFpEF animals; fluorescence transients obtained at colour-coded boxed locations are plotted to the right. CaT relaxation half-time ( $T_{1/2}$ ) at individual scan locations is overlaid in white. Black scale bars: vertical = 20  $\mu\text{m}$ , horizontal = 100 ms. B, mean (+ SD) uptake variability, calculated as the standard deviation of localized  $T_{1/2}$  at each spatial location along the scan line,  $n = 9$  cells from 3 control rats and 11 cells from three HFpEF rats. C, normalized diastolic fluo-4 fluorescence measured during action potentials recorded in current clamp at increasing frequencies in 14 cells from 3 control rats (blue bars) and 10 cells from 3 HFpEF rats (red bars). There was no statistically significant elevation in diastolic  $\text{Ca}^{2+}$  fluorescence in the HFpEF group compared to 0.2 Hz pacing rate. Statistics are calculated as Student's two-tailed unpaired *t* test (B) and two-way ANOVA (C). [Colour figure can be viewed at [wileyonlinelibrary.com](http://wileyonlinelibrary.com)]

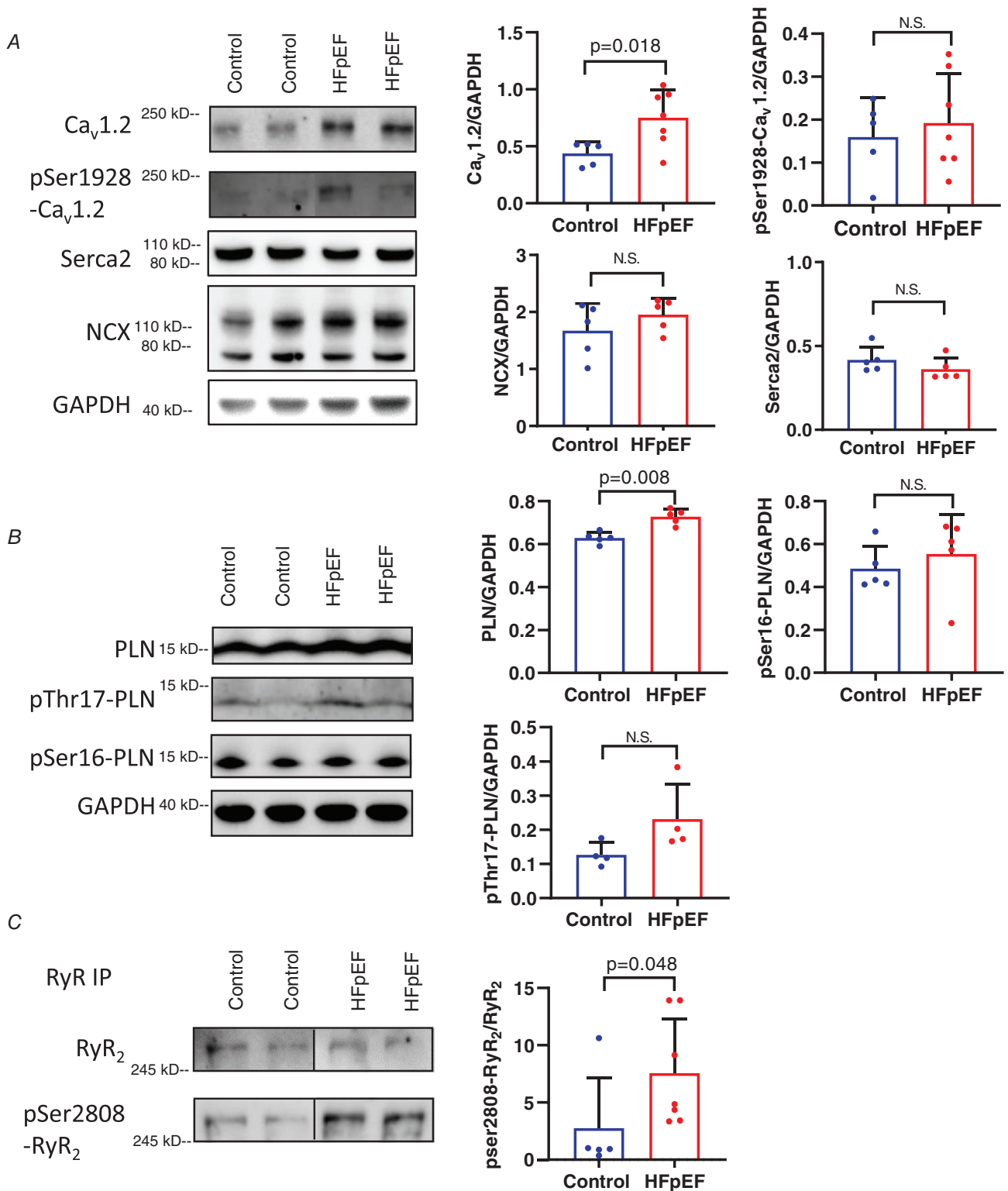


**Figure 8. Immunoblots of major Ca<sup>2+</sup>-handling proteins in HFpEF**  
 A and B, representative western blots from ventricular cardiomyocytes (left) and pooled data (right) showing mean density relative to GAPDH for major Ca<sup>2+</sup>-handling proteins (Ca<sub>v</sub>1.2, SERCA2, NCX and phospholamban (PLN) and assessment of phosphorylation at known sites (pSer1928 Ca<sub>v</sub>1.2, pThr17-PLN and pSer16-PLN). C, immunoprecipitation studies of RyR2 and pSer2808 RyR2 showing significant increase in phosphorylation of RyR2 relative to expression of RyR2. Data were normalized to RyR2 in the immunoprecipitated sample. Data expressed as means + SD. Statistics are calculated as Mann-Whitney rank test. [Colour figure can be viewed at [wileyonlinelibrary.com](http://wileyonlinelibrary.com)]

in HFpEF must be related to physiological changes in the behaviour and interactions of EC coupling proteins, e.g. LCCs and RyRs. Consistent with our findings, t-tubule disruption is not a prominent feature in HFpEF human heart tissue, unlike in HFrEF (Frisk *et al.* 2018).

Enhanced systolic function has been described in other models of HFpEF, including aged sheep (Dibb *et al.* 2004) and inbred hypertrophic heart rat (Curl *et al.* 2018). Similar changes in the amplitude and relaxation kinetics of the CaT have also been reported in rodent models of hypertrophy that lack the key features of HFpEF (specifically clinical signs and symptoms of severe heart failure associated with high mortality), including the spontaneously hypertensive rat (SHR) and a pressure overload rat model created by aortic banding (Delbridge *et al.* 1997; Shorofsky *et al.* 1999). Notably, increased  $I_{Ca}$  or blunted response to isoprenaline have not been reported in the SHR or aortic banding model, though increased efficacy of SR  $Ca^{2+}$  release triggered by  $I_{Ca}$  was noted in the SHR model (Shorofsky *et al.* 1999).

While we have focused this study on abnormal systolic function of HFpEF, the role of intracellular  $Ca^{2+}$  dynamics in the diastolic dysfunction of HFpEF requires discussion. Prior speculation (Loffredo *et al.* 2014) has posited that slowed  $Ca^{2+}$  reuptake into the SR contributes to impaired relaxation in HFpEF. Here we found no changes in global CaT decay rates in HFpEF using two different  $Ca^{2+}$  indicators in both patch-clamped and field stimulated cells. Furthermore, we did not observe any changes in  $Ca^{2+}$  efflux proteins or SERCA/PLB function. However, we did observe an increase in resting  $Ca^{2+}$ , an increased heterogeneity of  $Ca^{2+}$  uptake rates, and perhaps most importantly a pronounced deficit in global  $Ca^{2+}$  uptake that only became apparent upon stimulation with  $\beta$ -agonists. The increase in resting  $Ca^{2+}$  could contribute to increased resting stiffness based on binding kinetics to myofilaments. The reason for increased resting  $Ca^{2+}$  in HFpEF is not clear. Since we observed no change in NCX activity/expression or SERCA/PLB expression or phosphorylation (Fig. 8), we speculate that increased  $Ca^{2+}$  influx through LCCs together with increased  $Ca^{2+}$  leak by phosphorylated RyRs (Fig. 8) may be the cause (Wehrens *et al.* 2006; Dridi *et al.* 2020; Ke *et al.* 2020). Since we used the same  $Na^+$  concentration in our internal pipette solution for control and HFpEF studies, it seems unlikely that changes in intracellular  $Na^+$  can be invoked as a cause of reduced  $Ca^{2+}$  efflux by NCX. We also did not assess the activity or expression of the alternative  $Ca^{2+}$  efflux protein, the plasma membrane  $Ca^{2+}$  ATPase. Dissection of the mechanism(s) of elevated diastolic  $Ca^{2+}$  will require further study.

A lack of  $\beta$ -adrenergic reserve was similarly seen in the diminished enhancement of  $I_{Ca}$  and CaT amplitude in response to ISO. In normal cardiomyocytes, the PKA signalling cascade extensively alters cardiac function, both

acutely through the phosphorylation of ion-handling proteins, and chronically through altered gene expression. In EC coupling, activation through PKA results in increased phosphorylation of a multitude of ion channels, transporters and intimately associated regulators (LCC, RYR2, PLN, PDEs, AKAPs, Ahnak) (Boullaran & Gales, 2015) with the composite function of enhancing SR  $Ca^{2+}$  release and uptake during the cardiac cycle. We found no increase in baseline phosphorylation of  $Ca_v1.2$  (Fig. 8A) that might blunt further increase in current with ISO. Prior studies in the DS rat HFpEF model found no sarcolemmal downregulation of the  $\beta_1$ -adrenergic receptor or enhanced translocation of  $\beta$ ARK1/GRK2 in the heart (Nishio *et al.* 2008). This starkly contrasts with HFrEF, in which  $\beta_1$  receptor downregulation is a key feature of the disease (Lohse *et al.* 2003). These differences suggest a novel mode of regulation of the  $\beta$ -adrenergic/PKA signalling pathway in HFpEF, which we will address in future studies.

### Limitations

Both our HFpEF and HFrEF models display the key features of heart failure: increased left atrial size, pulmonary congestion (i.e. increased lung/body weight ratio) and decreased exercise tolerance (Borlaug & Redfield, 2011). While our rat model of HFpEF possesses a phenotype generally consistent with the human disease, extrapolation of any animal model findings to the human condition must be approached with caution. Certain aspects of  $Ca^{2+}$  handling and electrophysiological mechanisms are different in rats compared to larger animals, especially humans. For example, the action potential duration in the rat is far shorter than in humans, providing an abbreviated time for  $Ca^{2+}$  to enter the cell through  $Ca^{2+}$  channels. Nevertheless, key aspects of EC coupling remain conserved across species, including the CICR mechanism and its dependence upon the close association between t-tubules and RyRs on SR membranes (Eisner *et al.* 2017). Decreased t-tubule density and disorganization have been observed in HFrEF across many models and species (Swift *et al.* 2008; Heinzel *et al.* 2008; Lyon *et al.* 2009), but not in HFpEF (Frisk *et al.* 2018).

We chose the DS rat model because it has the virtue of having two comorbid features commonly found in human HFpEF: hypertension and insulin resistance. Models encompassing even greater multi-system maladaptation have been developed recently (Schiattarella *et al.* 2019), though none in which calcium handling and EC coupling have been rigorously examined as in the present work. Expanding our findings into other HFpEF models, particularly humans, should be a priority in future studies.

We chose the SD rat for generation of HFrEF via infarct because SD rats are the parent strain of DS rats (Rapp & Dene, 1985). This also had the advantage of allowing us to use DS rats fed a low-salt diet as controls for cellular

studies comparing HFrEF to HFpEF. Notably, sham surgery control SD rats had nearly identical morphometric parameters to low-salt fed DS rats. Thus, the latter served as control for most of the cellular studies we performed in both HFpEF and HFrEF. Although our rat infarct model of HFrEF displayed reduced systolic function, we found incomplete echocardiographic evidence of the diastolic dysfunction (decreased  $E/A$  but no change in  $E/e'$ ; Fig. 1*E*, *F* and *I*) reported by other groups (Litwin *et al.* 1994; Prunier *et al.* 2002). Since our goal was to use the infarct model to compare CICR as it relates to systolic function in HFpEF with HFrEF, the lack of demonstrable diastolic dysfunction does not detract from our key results: systolic function in HFrEF is characterized by defective EC coupling while systolic function in HFpEF is characterized by enhanced EC coupling. The lack of pacing-induced increases of diastolic  $Ca^{2+}$  in isolated HFpEF myocytes (Fig. 7*C*) may be explained by the relatively low pacing rates, bath ( $Ca^{2+}$ ) and temperature, conditions that were used to preserve cell viability during the long experiments.

Using the gold standard ratiometric  $Ca^{2+}$  indicator fura-2, we detected a  $Ca^{2+}$  handling signature in HFrEF myocytes consistent with the literature (decreased CaT amplitude, increased diastolic  $Ca^{2+}$  concentration). Analysis of raw fluo-4  $Ca^{2+}$  measurements revealed a significant decrease in caffeine-induced SR  $Ca^{2+}$  release in HFrEF, similar to what has been reported by others using fluo-4 (Gomez *et al.* 2001). However, we decided to be extraordinarily conservative about this non-ratiometric data and corrected it for the increased diastolic  $Ca^{2+}$  we had observed in the separate fura-2 experiments, as the ensuing  $\Delta F/F_0$  calculations are highly sensitive to resting fluorescence values. This unique approach is uncommon because it is rare to have the availability of diastolic information from parallel experiments using fura-2. Consequently, we found there was only a trend for reduction in caffeine-induced  $Ca^{2+}$  release (e.g. SR  $Ca^{2+}$  load;  $p = 0.145$ ) in HFrEF. We conclude from our experiments that t-tubule remodelling (and presumably orphan RyR2s) is the primary contributor to dyssynchronous  $Ca^{2+}$  release in the rat infarct HFrEF model, which is already well established (Song *et al.* 2006). If the reduction in SR load had been significant, it would have further reduced the extent of  $Ca^{2+}$  release and EC coupling gain, exaggerating the already-dramatic difference we observe in EC coupling between HFpEF and HFrEF. Notably, in the metabolic inhibition model of ischaemia, SR content is preserved but EC coupling fidelity is significantly reduced (Chantawansri *et al.* 2008).

## Conclusions

Our results highlight fundamental differences in EC coupling, cytoarchitecture,  $Ca^{2+}$  handling and integrative

pump function between HFpEF and HFrEF. Systolic function in HFpEF is normal or enhanced at baseline, reflecting increased  $I_{Ca}$ , a maximum degree of coupling fidelity, intact t-tubules and preserved global SR  $Ca^{2+}$  uptake. Relaxation in HFpEF may be impaired by the marked spatiotemporal inhomogeneity of  $Ca^{2+}$  decay throughout the myocyte in combination with non- $Ca^{2+}$ -dependent mechanisms such as increased collagen deposition and altered titin phosphorylation. Beyond these baseline abnormalities, the blunted cellular response to  $\beta$ -adrenergic stimulation is an important feature in this HFpEF model, which helps explain why common therapies to improve cardiac performance in HFrEF lack clinical efficacy in HFpEF.

## References

- Borlaug BA, Olson TP, Lam CS, Flood KS, Lerman A, Johnson BD & Redfield MM (2010). Global cardiovascular reserve dysfunction in heart failure with preserved ejection fraction. *J Am Coll Cardiol* **56**, 845–854.
- Borlaug BA & Redfield MM (2011). Diastolic and systolic heart failure are distinct phenotypes within the heart failure spectrum. *Circulation* **123**, 2006–2014; discussion 2014.
- Boullaran C & Gales C (2015). Cardiac cAMP: production, hydrolysis, modulation and detection. *Front Pharmacol* **6**, 203.
- Bryant SM, Kong CH, Watson J, Cannell MB, James AF & Orchard CH (2015). Altered distribution of  $I_{Ca}$  impairs Ca release at the t-tubules of ventricular myocytes from failing hearts. *J Mol Cell Cardiol* **86**, 23–31.
- Cain BS, Meldrum DR, Joo KS, Wang JF, Meng X, Cleveland JC Jr, Banerjee A & Harken AH (1998). Human SERCA2a levels correlate inversely with age in senescent human myocardium. *J Am Coll Cardiol* **32**, 458–467.
- Chantawansri C, Huynh N, Yamanaka J, Garfinkel A, Lamp ST, Inoue M, Bridge JH & Goldhaber JI (2008). Effect of metabolic inhibition on coupling behavior in rabbit ventricular myocytes. *Biophys J* **94**, 1656–1666.
- Cheng H, Song LS, Shirokova N, Gonzalez A, Lakatta EG, Rios E & Stern MD (1999). Amplitude distribution of calcium sparks in confocal images: theory and studies with an automatic detection method. *Biophys J* **76**, 606–617.
- Cho JH, Kilfoil PJ, Zhang R, Solymani RE, Bresee C, Kang EM, Luther K, Rogers RG, de Couto G, Goldhaber JI, Marban E & Cingolani E (2018*a*). Reverse electrical remodeling in rats with heart failure and preserved ejection fraction. *JCI Insight* **3**, e121123.
- Cho JH, Zhang R, Aynaszyan S, Holm K, Goldhaber JI, Marban E & Cingolani E (2018*b*). Ventricular arrhythmias underlie sudden death in rats with heart failure and preserved ejection fraction. *Circ Arrhythm Electrophysiol* **11**, e006452.
- Cho JH, Zhang R, Kilfoil PJ, Gallet R, de Couto G, Bresee C, Goldhaber JI, Marban E & Cingolani E (2017). Delayed repolarization underlies ventricular arrhythmias in rats with heart failure and preserved ejection fraction. *Circulation* **136**, 2037–2050.

- Curl CL, Danes VR, Bell JR, Raaijmakers AJA, Ip WTK, Chandramouli C, Harding TW, Porrello ER, Erickson JR, Charchar FJ, Kompa AR, Edgley AJ, Crossman DJ, Soeller C, Mellor KM, Kalman JM, Harrap SB & Delbridge LMD (2018). Cardiomyocyte functional etiology in heart failure with preserved ejection fraction is distinctive—a new preclinical model. *J Am Heart Assoc* **7**, e007451.
- Delbridge LM, Satoh H, Yuan W, Bassani JW, Qi M, Ginsburg KS, Samarel AM & Bers DM (1997). Cardiac myocyte volume,  $Ca^{2+}$  fluxes, and sarcoplasmic reticulum loading in pressure-overload hypertrophy. *Am J Physiol Heart Circ Physiol* **272**, H2425–H2435.
- Dibb KM, Rueckschloss U, Eisner DA, Isenberg G & Trafford AW (2004). Mechanisms underlying enhanced cardiac excitation contraction coupling observed in the senescent sheep myocardium. *J Mol Cell Cardiol* **37**, 1171–1181.
- Dridi H, Kushnir A, Zalk R, Yuan Q, Melville Z & Marks AR (2020). Intracellular calcium leak in heart failure and atrial fibrillation: a unifying mechanism and therapeutic target. *Nat Rev Cardiol* (in press); <https://doi.org/10.1038/s41569-020-0394-8>.
- Dunlay SM, Roger VL & Redfield MM (2017). Epidemiology of heart failure with preserved ejection fraction. *Nat Rev Cardiol* **14**, 591–602.
- Eisner D, Caldwell J & Trafford A (2013). Sarcoplasmic reticulum Ca-ATPase and heart failure 20 years later. *Circ Res* **113**, 958–961.
- Eisner DA, Caldwell JL, Kistamas K & Trafford AW (2017). Calcium and excitation-contraction coupling in the heart. *Circ Res* **121**, 181–195.
- Frisk M, Le C, Dahl CP, Lunde IG, Almaas VM, Gullestad L, Aakhus S, Sejersted OM, Tonnessen T & Louch WE (2018). T-tubule loss is a prominent feature of HFpEF but not HFpEF. *Biophys J* **114**, 618A–618A.
- Frisk M, Ruud M, Espe EK, Aronsen JM, Roe AT, Zhang L, Norseng PA, Sejersted OM, Christensen GA, Sjaastad I & Louch WE (2016). Elevated ventricular wall stress disrupts cardiomyocyte t-tubule structure and calcium homeostasis. *Cardiovasc Res* **112**, 443–451.
- Gallet R, de Couto G, Simsoló E, Valle J, Sun B, Liu W, Tselioui E, Zile MR & Marban E (2016). Cardiosphere-derived cells reverse heart failure with preserved ejection fraction (HFpEF) in rats by decreasing fibrosis and inflammation. *JACC Basic Transl Sci* **1**, 14–28.
- Gomez AM, Guatimosim S, Dilly KW, Vassort G & Lederer WJ (2001). Heart failure after myocardial infarction: altered excitation-contraction coupling. *Circulation* **104**, 688–693.
- Groenke S, Larson ED, Alber S, Zhang R, Lamp ST, Ren X, Nakano H, Jordan MC, Karagueuzian HS, Roos KP, Nakano A, Proenza C, Philipson KD & Goldhaber JJ (2013). Complete atrial-specific knockout of sodium-calcium exchange eliminates sinoatrial node pacemaker activity. *PLoS One* **8**, e81633.
- Grundy D (2015). Principles and standards for reporting animal experiments in *The Journal of Physiology* and *Experimental Physiology*. *J Physiol* **593**, 2547–2549.
- Guazzi M, Brenner DA, Apstein CS & Saupe KW (2001). Exercise intolerance in rats with hypertensive heart disease is associated with impaired diastolic relaxation. *Hypertension* **37**, 204–208.
- Guo A & Song LS (2014). AutoTT: automated detection and analysis of T-tubule architecture in cardiomyocytes. *Biophys J* **106**, 2729–2736.
- Hamdani N, Franssen C, Lourenco A, Falcao-Pires I, Fontoura D, Leite S, Plettig L, Lopez B, Ottenheim CA, Becher PM, Gonzalez A, Tschope C, Diez J, Linke WA, Leite-Moreira AF & Paulus WJ (2013). Myocardial titin hypophosphorylation importantly contributes to heart failure with preserved ejection fraction in a rat metabolic risk model. *Circ Heart Fail* **6**, 1239–1249.
- Heinzel FR, Bito V, Biesmans L, Wu M, Detre E, von Wegner F, Claus P, Dymarkowski S, Maes F, Bogaert J, Rademakers F, D'Hooge J & Sipido K (2008). Remodeling of T-tubules and reduced synchrony of  $Ca^{2+}$  release in myocytes from chronically ischemic myocardium. *Circ Res* **102**, 338–346.
- Hohendanner F, Ljubojevic S, MacQuaide N, Sacherer M, Sedej S, Biesmans L, Wakula P, Platzer D, Sokolow S, Herchuelz A, Antoons G, Sipido K, Pieske B & Heinzel FR (2013). Intracellular dyssynchrony of diastolic cytosolic ( $Ca^{2+}$ ) decay in ventricular cardiomyocytes in cardiac remodeling and human heart failure. *Circ Res* **113**, 527–538.
- Hong T & Shaw RM (2017). Cardiac t-tubule microanatomy and function. *Physiol Rev* **97**, 227–252.
- Hulot JS, Salem JE, Redheuil A, Collet JP, Varnous S, Jourdain P, Logeart D, Gandjbakhch E, Bernard C, Hatem SN, Isnard R, Cluzel P, Le Feuvre C, Leprince P, Hammoudi N, Lemoine FM, Klatzmann D, Vicaute E, Komajda M, Montalescot G, Lompre AM, Hajjar RJ & Investigators A-H (2017). Effect of intracoronary administration of AAV1/SERCA2a on ventricular remodeling in patients with advanced systolic heart failure: results from the AGENT-HF randomized phase 2 trial. *Eur J Heart Fail* **19**, 1534–1541.
- Inoue M & Bridge JH (2003).  $Ca^{2+}$  sparks in rabbit ventricular myocytes evoked by action potentials: involvement of clusters of L-type  $Ca^{2+}$  channels. *Circ Res* **92**, 532–538.
- Ke HY, Yang HY, Francis AJ, Collins TP, Surendran H, Alvarez-Laviada A, Firth JM & MacLeod KT (2020). Changes in cellular  $Ca^{2+}$  and  $Na^{+}$  regulation during the progression towards heart failure in the guinea pig. *J Physiol* **598**, 1339–1359.
- Kockskamper J, Sheehan KA, Bare DJ, Lipsius SL, Mignery GA & Blatter LA (2001). Activation and propagation of  $Ca^{2+}$  release during excitation-contraction coupling in atrial myocytes. *Biophys J* **81**, 2590–2605.
- Lam CSP, Gamble GD, Ling LH, Sim D, Leong KTG, Yeo PSD, Ong HY, Jaueferally F, Ng TP, Cameron VA, Poppe K, Lund M, Devlin G, Troughton R, Richards AM & Doughty RN (2018). Mortality associated with heart failure with preserved vs. reduced ejection fraction in a prospective international multi-ethnic cohort study. *Eur Heart J* **39**, 1770–1780.
- Litwin SE, Katz SE, Morgan JP & Douglas PS (1994). Serial echocardiographic assessment of left ventricular geometry and function after large myocardial infarction in the rat. *Circulation* **89**, 345–354.
- Litwin SE, Zhang D & Bridge JH (2000). Dyssynchronous  $Ca^{2+}$  sparks in myocytes from infarcted hearts. *Circ Res* **87**, 1040–1047.
- Loffredo FS, Nikolova AP, Pancoast JR & Lee RT (2014). Heart failure with preserved ejection fraction: molecular pathways of the aging myocardium. *Circ Res* **115**, 97–107.

- Lohse MJ, Engelhardt S & Eschenhagen T (2003). What is the role of beta-adrenergic signaling in heart failure? *Circ Res* **93**, 896–906.
- Louch WE, Mork HK, Sexton J, Stromme TA, Laake P, Sjaastad I & Sejersted OM (2006). T-tubule disorganization and reduced synchrony of Ca<sup>2+</sup> release in murine cardiomyocytes following myocardial infarction. *J Physiol* **574**, 519–533.
- Lyon AR, MacLeod KT, Zhang Y, Garcia E, Kanda GK, Lab MJ, Korchev YE, Harding SE & Gorelik J (2009). Loss of T-tubules and other changes to surface topography in ventricular myocytes from failing human and rat heart. *Proc Natl Acad Sci U S A* **106**, 6854–6859.
- Marks AR (2013). Calcium cycling proteins and heart failure: mechanisms and therapeutics. *J Clin Invest* **123**, 46–52.
- Nishio M, Sakata Y, Mano T, Ohtani T, Takeda Y, Miwa T, Hori M, Masuyama T, Kondo T & Yamamoto K (2008). Beneficial effects of bisoprolol on the survival of hypertensive diastolic heart failure model rats. *Eur J Heart Fail* **10**, 446–453.
- Norman HS, Oujiri J, Larue SJ, Chapman CB, Margulies KB & Sweitzer NK (2011). Decreased cardiac functional reserve in heart failure with preserved systolic function. *J Card Fail* **17**, 301–308.
- Ogihara T, Asano T, Ando K, Sakoda H, Anai M, Shojima N, Ono H, Onishi Y, Fujishiro M, Abe M, Fukushima Y, Kikuchi M & Fujita T (2002). High-salt diet enhances insulin signaling and induces insulin resistance in Dahl salt-sensitive rats. *Hypertension* **40**, 83–89.
- Ouzounian M, Lee DS & Liu PP (2008). Diastolic heart failure: mechanisms and controversies. *Nat Clin Pract Cardiovasc Med* **5**, 375–386.
- Pfeffer MA, Pfeffer JM, Fishbein MC, Fletcher PJ, Spadaro J, Kloner RA & Braunwald E (1979). Myocardial infarct size and ventricular function in rats. *Circ Res* **44**, 503–512.
- Pieske B, Tschope C, de Boer RA, Fraser AG, Anker SD, Donal E, Edelmann F, Fu M, Guazzi M, Lam CSP, Lancellotti P, Melenovsky V, Morris DA, Nagel E, Pieske-Kraigher E, Ponikowski P, Solomon SD, Vasan RS, Rutten FH, Voors AA, Ruschitzka F, Paulus WJ, Seferovic P & Filippatos G (2019). How to diagnose heart failure with preserved ejection fraction: the HFA-PEFF diagnostic algorithm: a consensus recommendation from the Heart Failure Association (HFA) of the European Society of Cardiology (ESC). *Eur Heart J* **40**, 3297–3317.
- Porzig H, Li Z, Nicoll DA & Philipson KD (1993). Mapping of the cardiac sodium-calcium exchanger with monoclonal antibodies. *Am J Physiol Cell Physiol* **265**, C748–C756.
- Prunier F, Gaertner R, Louedec L, Michel JB, Mercadier JJ & Escoubet B (2002). Doppler echocardiographic estimation of left ventricular end-diastolic pressure after MI in rats. *Am J Physiol Heart Circ Physiol* **283**, H346–H352.
- Rapp JP & Dene H (1985). Development and characteristics of inbred strains of Dahl salt-sensitive and salt-resistant rats. *Hypertension* **7**, 340–349.
- Schiattarella GG, Altamirano F, Tong D, French KM, Villalobos E, Kim SY, Luo X, Jiang N, May HI, Wang ZV, Hill TM, Mammen PPA, Huang J, Lee DI, Hahn VS, Sharma K, Kass DA, Lavandro S, Gillette TG & Hill JA (2019). Nitrosative stress drives heart failure with preserved ejection fraction. *Nature* **568**, 351–356.
- Shah KS, Xu H, Matsouaka RA, Bhatt DL, Heidenreich PA, Hernandez AF, Devore AD, Yancy CW & Fonarow GC (2017). Heart failure with preserved, borderline, and reduced ejection fraction: 5-year outcomes. *J Am Coll Cardiol* **70**, 2476–2486.
- Shorofsky SR, Aggarwal R, Corretti M, Baffa JM, Strum JM, Al-Seikhan BA, Kobayashi YM, Jones LR, Wier WG & Balke CW (1999). Cellular mechanisms of altered contractility in the hypertrophied heart: big hearts, big sparks. *Circ Res* **84**, 424–434.
- Song LS, Sobie EA, McCulle S, Lederer WJ, Balke CW & Cheng H (2006). Orphaned ryanodine receptors in the failing heart. *Proc Natl Acad Sci U S A* **103**, 4305–4310.
- Swift F, Birkeland JA, Tovsrud N, Enger UH, Aronsen JM, Louch WE, Sjaastad I & Sejersted OM (2008). Altered Na<sup>+</sup>/Ca<sup>2+</sup>-exchanger activity due to downregulation of Na<sup>+</sup>/K<sup>+</sup>-ATPase alpha2-isoform in heart failure. *Cardiovasc Res* **78**, 71–78.
- Terrovitis J, Lautamaki R, Bonios M, Fox J, Engles JM, Yu J, Leppo MK, Pomper MG, Wahl RL, Seidel J, Tsui BM, Bengel FM, Abraham MR & Marban E (2009). Noninvasive quantification and optimization of acute cell retention by in vivo positron emission tomography after intramyocardial cardiac-derived stem cell delivery. *J Am Coll Cardiol* **54**, 1619–1626.
- Wang D, Liu T, Shi S, Li R, Shan Y, Huang Y, Hu D & Huang C (2016). Chronic administration of catestatin improves autonomic function and exerts cardioprotective effects in myocardial infarction rats. *J Cardiovasc Pharmacol Ther* **21**, 526–535.
- Wehrens XH, Lehnart SE, Reiken S, Vest JA, Wronska A & Marks AR (2006). Ryanodine receptor/calcium release channel PKA phosphorylation: a critical mediator of heart failure progression. *Proc Natl Acad Sci U S A* **103**, 511–518.
- Yue X, Zhang R, Kim B, Ma A, Philipson KD & Goldhaber JJ (2017). Heterogeneity of transverse-axial tubule system in mouse atria: Remodeling in atrial-specific Na<sup>+</sup>-Ca<sup>2+</sup> exchanger knockout mice. *J Mol Cell Cardiol* **108**, 50–60.
- Zile MR & Gaasch WH (2011). Abnormal calcium homeostasis: one mechanism in diastolic heart failure. *J Am Coll Cardiol* **58**, 155–157.
- Zima AV, Bovo E, Mazurek SR, Rochira JA, Li W & Terentyev D (2014). Ca handling during excitation-contraction coupling in heart failure. *Pflugers Arch* **466**, 1129–1137.

## Additional information

### Data availability statement

The data that support the findings of this study are available from the corresponding author upon reasonable request.

### Competing interests

None.

### Author contributions

P.J.K., E.M. and J.I.G. designed the protocols. P.J.K., S.L., R.Z., S.A. and R.E.S. conducted the experiments. P.J.K., S.L., R.Z., X.Y., S.A. and R.E.S. analysed the data and prepared the figures. P.J.K., E.C., E.M. and J.I.G. wrote and edited the article. All authors approved the final version of the article and agree to be accountable for all aspects of the work in ensuring that questions related to the accuracy or integrity of any part of the work are appropriately investigated and resolved. All persons designated as authors qualify for authorship, and all those who qualify for authorship are listed.

### Funding

This research was supported by National Institutes of Health grants T32 HL116273 to J.I.G. and E.M., HL048509 to J.I.G.,

R01 HL147570 to J.I.G. and E.C. and Department of Defense grant PR150620 to E.M.

### Keywords

$\beta$ -adrenergic stimulation, calcium, excitation-contraction coupling, HFpEF

### Supporting information

Additional supporting information may be found online in the Supporting Information section at the end of the article.

### Statistical Summary Document